ARTICLE

doi:10.1038/nature20824

Rational design of reconfigurable prismatic architected materials

Johannes T. B. Overvelde[1,2], James C. Weaver[3], Chuck Hoberman[3,4,5] & Katia Bertoldi[1,6]

Advances in fabrication technologies are enabling the production of architected materials with unprecedented properties. Most such materials are characterized by a fixed geometry, but in the design of some materials it is possible to incorporate internal mechanisms capable of reconfiguring their spatial architecture, and in this way to enable tunable functionality. Inspired by the structural diversity and foldability of the prismatic geometries that can be constructed using the snapology origami technique, here we introduce a robust design strategy based on space-filling tessellations of polyhedra to create three-dimensional reconfigurable materials comprising a periodic assembly of rigid plates and elastic hinges. Guided by numerical analysis and physical prototypes, we systematically explore the mobility of the designed structures and identify a wide range of qualitatively different deformations and internal rearrangements. Given that the underlying principles are scale-independent, our strategy can be applied to the design of the next generation of reconfigurable structures and materials, ranging from metre-scale transformable architectures to nanometre-scale tunable photonic systems.

In the search for materials with new properties, there have been great advances in recent years aimed at the construction of architected materials, whose behaviour is governed by structure, rather than composition[1–3]. Through careful design of the material's architecture, new material properties have been demonstrated, including negative index of refraction[4,5], negative Poisson's ratio[6], high stiffness-to-weight ratio[7,8] and optical[9] and mechanical[10] cloaking. However, most of the proposed architected materials (also known as metamaterials) have a unique structure that cannot be reconfigured after fabrication, making each metamaterial suitable only for a specific task and limiting its applicability to well known and controlled environments.

The ancient art of origami provides an ideal platform for the design of reconfigurable systems, since a myriad of shapes can be achieved by actively folding thin sheets along pre-defined creases. While most of the proposed origami-inspired metamaterials are based on two-dimensional folding patterns, such as the miura-ori[11–17], the square twist[18] and box-pleat tiling[19], it has been shown that cellular structures can be designed by stacking these folded layers[13], or assembling them in tubes[20–23]. Furthermore, taking inspiration from snapology[24,25]—a modular origami technique—a highly reconfigurable three-dimensional (3D) metamaterial assembled from extruded cubes has been designed[26]. Although these examples showcase the potential of origami-inspired designs to enable reconfigurable architected materials, they do not fully exploit the range of achievable deformations and cover only a small region of the available design space. As a result, ample opportunities for the design of architected materials with tunable responses remain.

Here, we introduce a robust strategy for the design of 3D reconfigurable architected materials and show that a wealth of responses can be achieved in periodic 3D assemblies of rigid plates connected by elastic hinges. To build these structures, we use periodic space-filling tessellations of convex polyhedra as templates, and extrude arbitrary combinations of the polygon faces. In an effort to design architected materials with specific properties, we systematically explore the proposed designs by performing numerical simulations and characterize the mobility (that is, number of degrees of freedom) of the systems. We find that qualitatively different responses can be achieved, including shear, uniform expansion along one or two principal directions, and internal reconfigurations that do not alter the macroscopic shape of the materials. Therefore, this research paves the way for a new class of structures that can tune their shape and function to adapt and even influence their surroundings, bringing origami-inspired metamaterials closer to application.

Design strategy

To design 3D reconfigurable architected materials, we start by selecting a space-filling and periodic assembly of convex polyhedra (Fig. 1). We then perform two operations on the tessellation. (i) We separate adjacent polyhedra while ensuring that the normals of the overlapping faces remain aligned. This can be achieved by imposing that for each overlapping face pair

$$d\boldsymbol{p}_{j,\mathrm{b}} - d\boldsymbol{p}_{j,\mathrm{a}} = 2L_j\boldsymbol{n}_j \tag{1}$$

where $d\boldsymbol{p}_j$ denotes the displacements applied to the polyhedra to separate the jth pair of faces, and the subscripts a and b indicate to which polyhedron the two overlapping faces belong. Moreover, L_j is the distance between the jth pair of faces in the separated state, and $\boldsymbol{n}_j$ is the unit normal to the faces pointing outward from the polyhedron indicated by the subscript a. (ii) We extrude the edges of the polyhedra in the direction normal to their faces to form a connected thin-walled structure (Fig. 1), which we refer to as a prismatic architected material (Supplementary Video 1).

Importantly, for the periodic space-filling tessellations considered here, it is sufficient to focus on a unit cell that consists of only a few polyhedra and covers the entire assembly when translated by the three lattice vectors $\boldsymbol{l}_i^0$ ($i = 1, 2, 3$). While equation (1) can be directly imposed on all internal face pairs in the unit cell, for overlapping faces that are periodically located (that is, lie on the external boundary of the unit cell) the constraint needs to be updated as

$$d\boldsymbol{p}_{j,\mathrm{b}} - d\boldsymbol{p}_{j,\mathrm{a}} + \boldsymbol{R}_j - \boldsymbol{R}_j^0 = 2L_j\boldsymbol{n}_j \tag{2}$$

[1]School of Engineering and Applied Sciences, Harvard University, Cambridge, Massachusetts 02138, USA. [2]AMOLF, Science Park 104, 1098XG Amsterdam, The Netherlands. [3]Wyss Institute for Biologically Inspired Engineering, Harvard University, Cambridge, Massachusetts 02138, USA. [4]Hoberman Associates, New York, New York 10001, USA. [5]Graduate School of Design, Harvard University, Cambridge, Massachusetts 02138, USA. [6]Kavli Institute, Harvard University, Cambridge, Massachusetts 02138, USA.

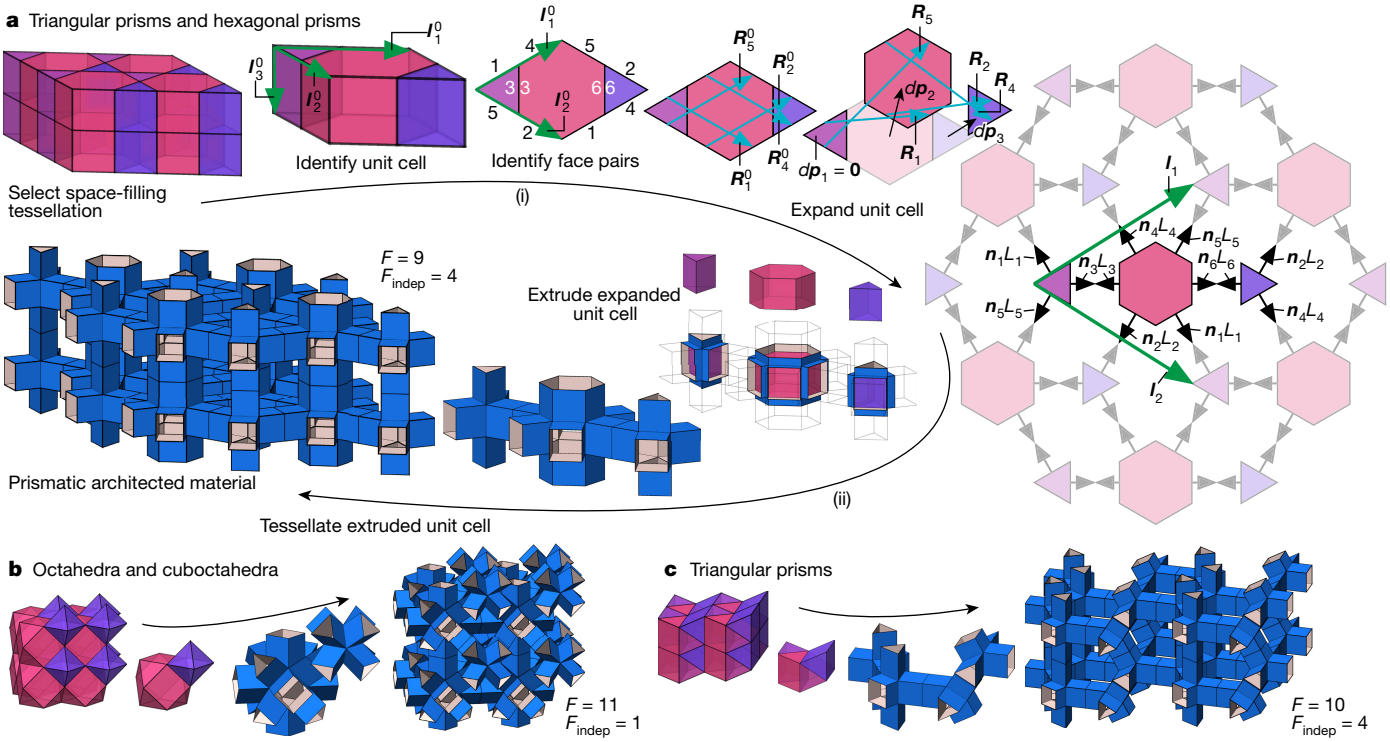

Figure 1 | Design strategy to construct 3D prismatic architected materials. Space-filling and periodic assemblies of convex polyhedra are used as templates to construct prismatic architected materials (Supplementary Video 1). After selecting a space-filling tessellation, we focus on a unit cell spanned by the three lattice vectors $\boldsymbol{l}_i^0$ ($i = 1, 2, 3$) and identify all pairs of overlapping faces. We then separate the polyhedra while ensuring that the normals of all face pairs remain aligned. Finally, we extrude the edges of the polyhedra in the direction normal to their faces to construct the extruded unit cell. Note that the architected material can be constructed by tessellating the extruded unit cell along the three new lattice vectors $\boldsymbol{l}_i$. Using this approach, we designed three architected materials that are based on space-filling tessellations comprising triangular prisms and hexagonal prisms (**a**), octahedra and cuboctahedra (**b**) and triangular prisms (**c**).

where $\boldsymbol{R}_j = \sum_{i=1}^{3} \alpha_{j,i} \boldsymbol{l}_i$ and $\boldsymbol{R}_j^0 = \sum_{i=1}^{3} \alpha_{j,i} \boldsymbol{l}_i^0$ denote the distance between the two periodically located faces in the expanded and initial configuration, respectively, $\boldsymbol{l}_i$ being the lattice vectors of the expanded unit cell and $\alpha_{j,i} \in \{-1, 0, 1\}$. As shown by equations (1) and (2), for a unit cell with F face pairs the expanded configuration is fully described by F extrusion lengths L_j ($j = 1, \ldots, F$) (Fig. 1). However, for most unit cells the extrusion lengths cannot all be specified independently owing to the constraints introduced by equations (1) and (2). As a result, each unit cell is characterized by $F_{\text{indep}} \leq F$ independent extrusion lengths as illustrated in Supplementary Fig. 6. For the sake of convenience we chose the F_{indep} independent extrusion lengths to be as close as possible to an average extrusion length $\overline{L}$, by solving

$$\min_{L_1 \ldots L_{F_{\text{indep}}}} \quad \sum_{j=1}^{F} (L_j - \overline{L})^2 \tag{3}$$

while ensuring that the constraints imposed by equations (1) and (2) are not violated.

Finally, we note that all periodic and space-filling assemblies of convex polyhedra tested in this study were successfully extruded following the proposed design strategy (that is, we always found $F_{\text{indep}} \geq 1$). As an example, in Fig. 1 we show three prismatic architected materials based on unit cells containing two triangular and one hexagonal prism (Fig. 1a), an octahedron and cuboctahedron (Fig. 1b), and four triangular prisms (Fig. 1c).

Characterizing reconfigurability

Although the aforementioned design strategy represents a robust and efficient approach to construct prismatic architected materials, it does not provide any indication of their reconfigurability. To determine whether, and to what extent, the meso-structure of the designed architected materials can be reshaped, we started by fabricating centimetre-scale prototypes from cardboard and double-sided tape (Fig. 2a–c), using a stepwise layering and laser-cutting technique (see the 'Methods' subsection of Supplementary Information)[26,27].

Focusing on the three architected materials shown in Fig. 1, we find that the structure based on triangular prisms and the one based on a combination of triangular and hexagonal prisms can be reconfigured by bending the edges and without deforming the faces, and are respectively characterized by one and two deformation modes (Fig. 2d, e and Supplementary Video 2). In contrast, the material based on a combination of octahedra and cuboctahedra is completely rigid (Fig. 2b and Supplementary Video 2). Furthermore, our experiments reveal that these architected materials have fewer degrees of freedom than their constituent individual extruded polyhedra (Supplementary Fig. 7), indicating that the additional constraints introduced by the connections between the polyhedra effectively reduce their reconfigurability.

Numerical algorithm

While the examples of Fig. 2a–e illustrate the potential of our strategy to design reconfigurable architected materials, they also show that the design of systems with specific behaviour is not straightforward. To improve our understanding of the reconfigurability of the proposed architected materials, we implemented a numerical algorithm that predicts their mobility and corresponding deformation modes. In our numerical analysis, each extruded unit cell is modelled as a set of rigid faces connected by linear torsional springs, with periodic boundary conditions applied to the vertices located on the boundaries. To characterize the mobility of the structure we solved the following eigen-problem $\widetilde{M}^{-1}\widetilde{K}\boldsymbol{a}_{\text{m}} = \omega^2 \boldsymbol{a}_{\text{m}}$, in which $\widetilde{M}$ and $\widetilde{K}$ are respectively the mass and stiffness matrices, which account for both the rigidity of the faces and the periodic boundary conditions through master–slave elimination. Moreover, ω is an eigenfrequency of the system and $\boldsymbol{a}_{\text{m}}$ is the amplitude of the corresponding mode (see the 'Mode analysis for

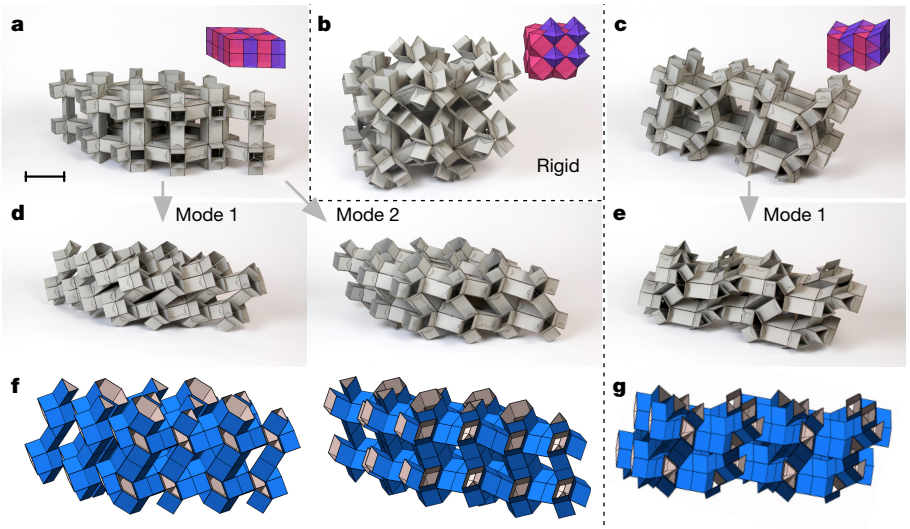

Figure 2 | Deformation modes of 3D prismatic architected materials. **a**–**c**, Prototypes of the 3D prismatic architected materials shown in Fig. 1 were constructed using cardboard (rigid faces) and double-sided tape (flexible hinges). **d**, The structure based on a combination of triangular and hexagonal prisms can be reconfigured in two different ways (that is, has two degrees of freedom). **e**, The structure based on triangular prisms has a single deformation mode. Note that the architected material based on the octahedra and cuboctahedra cannot be reconfigured. **f**, **g**, Simulated modes of the reconfigurable architected materials. The obtained deformation modes were linearly scaled to match the experiments (scale bar in **a**, 10 cm).

3D prismatic architected materials with rigid faces' subsection of Supplementary Information).

Figure 2f, g shows the simulated eigenmodes for the two reconfigurable architected materials considered in Fig. 1a, c. Although the simulations predict only the deformation for small rotations, the modes are strikingly similar to the deformation observed in the experiments (Fig. 2d, e). Solving the aforementioned eigenproblem therefore provides a convenient approach to determine the mobility of the structures and gives insight into their deformation without the need for specific boundary conditions.

Designs based on uniform tessellations

To further explore the potential of prismatic architected materials, and to establish relations between their reconfigurability and the initial space-filling polyhedral assembly, we next focus on extruded materials based on the 28 uniform tessellations of the 3D space, which comprise regular polyhedra, semiregular polyhedra and semiregular prisms[28–30]. Owing to their relative simplicity, these uniform templates provide a convenient starting point to explore the design space.

Using the numerical algorithm, we first determined the number of degrees of freedom, n_{dof}, of the resulting 28 architected materials (Supplementary Fig. 9). We find that the mobility of the unit cells is affected by two parameters: the average connectivity of the unit cell, $\overline{z}=\frac{1}{P}\sum_{p=1}^{P} z_p$, and the average number of modes of the individual polyhedra, $\overline{n}=\frac{1}{P}\sum_{p=1}^{P} n_p$, where P is the number of polyhedra in the unit cell and z_p and n_p are the number of extruded faces and modes of the pth polyhedron, respectively (Supplementary Fig. 8). The results for the 28 architected materials reported in Fig. 3 show three key features. First, higher values for $\overline{z}$ lead to rigid materials (that is, $n_{\mathrm{dof}}=0$ for $\overline{z}>8$). Second, if all the constituent extruded polyhedra are rigid (that is, $\overline{n}=0$), the resulting architected material is rigid as well. Third, only 13 of the 28 designs are reconfigurable (that is, $n_{\mathrm{dof}}>0$).

Interestingly, we find that all of the 13 reconfigurable structures are based on unit cells comprising only prisms, such that they recover the relation previously demonstrated for extruded individual prisms, $\overline{n}=\overline{z}-3$ (ref. 31). Moreover, our results indicate that most of the reconfigurable structures are characterized by fewer degrees of freedom than the constituent individual polyhedra (that is, $n_{\mathrm{dof}}<\overline{n}$), with the exception of the architected materials based on the cube (number 22) and the triangular prism (number 11) for which $n_{\mathrm{dof}}=\overline{n}$.

Having determined the number of modes for the 28 architected materials, we next characterize the macroscopic deformation associated to each of them. More specifically, we determine the macroscopic volumetric strain $\delta=\sum_{j=1}^{3}\epsilon_j$ for each mode, where ϵ_j are the macroscopic principal strains (see the 'Mode analysis for 3D prismatic architected materials with rigid faces' subsection of Supplementary Information). Interestingly, we find that for the 13 reconfigurable architectures all modes are characterized by $\delta=0$, which indicates pure macroscopic shearing deformation, as also confirmed by visual inspection of the modes (Supplementary Fig. 9).

To characterize the reconfigurability of prismatic architected materials, so far we had assumed the faces to be completely rigid and

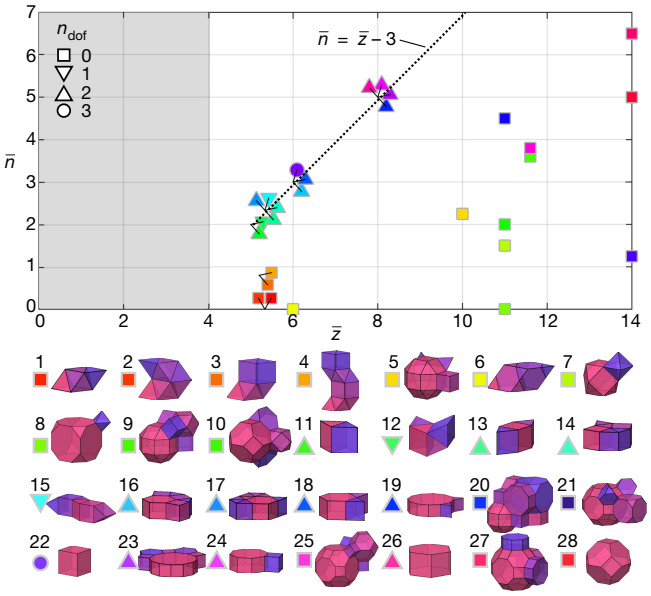

Figure 3 | Number of degrees of freedom for architected materials based on the 28 uniform tessellations of the 3D space. The mobility of the structures is affected by the average connectivity, $\overline{z}$, and the average mobility, $\overline{n}$. Overlapping data were separated for clarity; the small black lines indicate the original position of the data in each cluster. The prismatic architected materials and their deformation modes are shown in Supplementary Fig. 9.

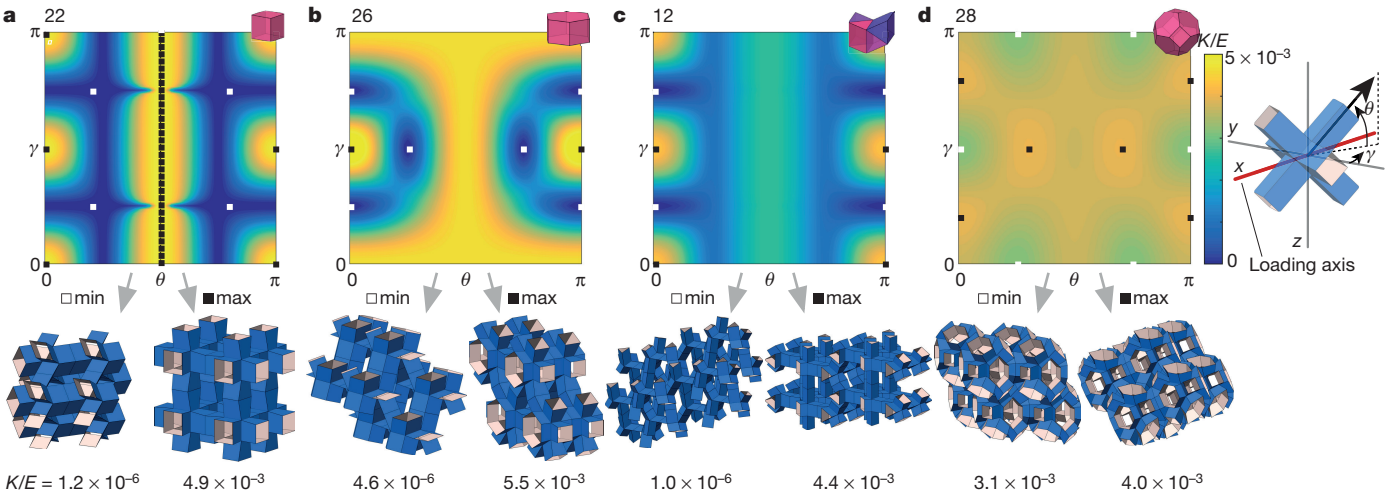

Figure 4 | Normalized stiffness *K*/*E* of prismatic architected materials. **a**–**d**, The results for architected materials based on template numbers 22 (**a**), 26 (**b**), 12 (**c**) and 28 (**d**). To determine the stiffness in all loading directions, the architected materials are rotated by angles γ and θ before loading. In each contour plot we indicate the minimum and maximum stiffness with white and black squares, respectively. We also show the deformed architected materials for the minimum and maximum stiffness direction. Note that the deformation is magnified to facilitate visualization.

the hinges to act as linear torsional springs. However, fabrication will always result in deformable faces, raising the question of whether prismatic architected materials can be reconfigured when their faces are deformable. To explore this direction, we updated our numerical algorithm by introducing a set of springs to account for the deformability of the faces[12,13,21] (see the 'Stiffness of 3D prismatic architected materials with deformable faces' subsection of Supplementary Information). We then deformed the extruded unit cells uniaxially and investigated their macroscopic stiffness for different loading directions (identified by the two angles γ and θ as shown in Fig. 4).

In Fig. 4 we report the normalized stiffness K/E as a function of γ and θ for four prismatic architected materials characterized by $t/\overline{L} = 0.01$, where E is the Young's modulus of the material and t is the thickness of the faces. We find that the response of the architected material based on template number 28, which was previously qualified as rigid (that is, $n_{\mathrm{dof}} = 0$), is fairly isotropic because its stiffness does not vary much as a function of the loading direction (that is, $3.1 \times 10^{-3} \leq K/E \leq 4.0 \times 10^{-3}$). In contrast, the stiffness of architected materials for which $n_{\mathrm{dof}} > 0$ drops noticeably for specific directions (that is, $K_{\min}/K_{\max} = \mathcal{O}(10^{-3})$). Interestingly, these are the loading directions for which the reconfiguring modes are activated, as indicated by the deformed structures shown in Fig. 4. Therefore, these results indicate that the deformation modes we found in the limit of rigid faces still persist even when the faces are deformable. We used the same stiffness for bending of the faces and bending of the hinges, and from the results we can therefore conclude that the architecture of these systems makes bending of the faces energetically costly (because it is typically accompanied by stretching and shearing of the faces). Finally, materials characterized by higher n_{dof} are characterized by more 'soft' deformation modes. As such, materials with $n_{\mathrm{dof}} = 1$ seem most promising for the design of reconfigurable architected materials, since they can be reconfigured along a specific direction, while still being able to carry loads in all other directions (Fig. 4 and Supplementary Fig. 10).

Enhancing the reconfigurability

Although we have shown that by extruding the edges of expanded assemblies of polyhedra we can construct reconfigurable architected materials, our results indicate that the mobility of the resulting structures is strongly reduced by their connectivity. Furthermore, the modes of all reconfigurable designs show a qualitatively similar shearing deformation. To overcome these limitations, we next introduce an additional step in the design strategy and reduce the connectivity of the materials by extruding some of the faces of the unit cell, while making the remaining faces rigid.

As an example, in Fig. 5 we consider the architected material based on a tessellation of truncated octahedra (number 28). When all faces are extruded, $\overline{z}=14$, leaving the structure rigid (that is, $n_{\mathrm{dof}} = 0$). However, by making 8 of the 14 faces rigid instead of extruding them (Fig. 5a and Supplementary Video 3) we can reduce the connectivity to $\overline{z}=6$ and the resulting architected material is no longer rigid, because $n_{\mathrm{dof}} = 1$. As shown in Fig. 5b and Supplementary Video 3, this response was also confirmed experimentally. Finally, we note that by varying the face pairs in the unit cell that are made rigid instead of extruded, a total of $2^F = 128$ different architected materials can be designed using the truncated octahedra as a template. However, only 82 combinations are possible (as all the other cases will result in structures with disconnected parts) and of those designs only four are reconfigurable. Owing to symmetries in the truncated octahedron, these four configurations are identical to the one shown in Fig. 5.

Next, to determine the range of deformations that can be achieved in the proposed structures, we apply the same brute force strategy to the other 27 uniform space-filling tessellations depicted in Fig. 3. For this study we considered a maximum of 2^{16} designs per tessellation, randomly selected from the 2^F possibilities, so that for 11 of the tessellations (numbers 4, 5, 9, 10, 16, 17, 20, 21, 23, 25 and 27) the results are not complete, but rather indicate a trend. We expanded the number of possible designs by removing the polyhedra for which all faces have been made rigid from the extruded unit cell, because those would have resulted in rigid parts completely disconnected from the architected materials.

Of the approximately 0.6×10^6 connected designs investigated here (Supplementary Table 1), 90% are rigid (that is, $n_{\mathrm{dof}} = 0$) while the other 10% are reconfigurable (that is, $n_{\mathrm{dof}} > 0$). Supplementary Fig. 11a, b shows that to achieve reconfigurability we still need $\overline{z} \leq 8$, with the exception of six designs based on number 5 for which $\overline{z} = 9$ (see Supplementary Fig. 12). Moreover, fully extruded architected materials characterized by $\overline{n} = 0$ always remain rigid, independent of the reduced number of connections. Finally, and perhaps more importantly, we also find that using this design approach the mobility of the architected materials can be greatly enhanced, as $0 \leq n_{\mathrm{dof}} \leq 16$ and for many of the structures $n_{\mathrm{dof}} > \overline{n}$ (Supplementary Table 1).

Inspection of the modes also reveals that a variety of qualitatively different types of deformation can be achieved. To characterize them better, in Fig. 6 and Supplementary Fig. 11c–f we report the magnitude

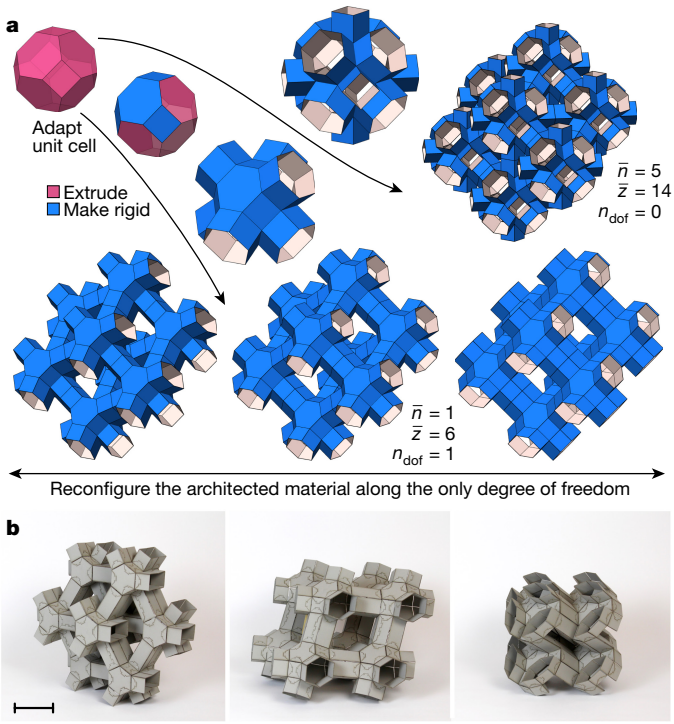

Figure 5 | Enhancing the reconfigurability of 3D prismatic architected materials. a, To enhance the reconfigurability of the architected material based on the space-filling assembly of truncated octahedra (number 28 in Fig. 3), we extrude only six of its faces and make the remaining eight faces rigid. Using this approach, the average connectivity is reduced from $\bar{z}=14$ to $\bar{z}=6$ and the resulting structure is no longer rigid, because $n_{dof}=1$. **b**, Experimental validation of the numerical predictions (scale bar, 10 cm).

of the principal strains, $\|\epsilon\|=\sqrt{\sum_{i=1}^{3}\epsilon_i^2}$, versus the volumetric strain, δ, for each deformation mode observed in the reconfigurable architected materials investigated here. Interestingly, we find that for many modes $\|\epsilon\|=\delta=0$. These modes do not alter the global shape of the structure, but result only in internal rearrangements. The design labelled a, shown in Fig. 6, is an example of a structure undergoing such a local deformation. Here, most of the structure is rigid except for one-dimensional tubes that can deform independently. In contrast, the design labelled b is an example in which the whole internal structure is deforming, while maintaining the same macroscopic shape (Supplementary Video 4).

Besides these local modes, Fig. 6 also indicates that there are designs capable of achieving types of macroscopic deformation that differ from pure shear (for which $\delta=0$ and $\|\epsilon\|>0$). For example, we find that some of the structures are characterized by an effective vanishing strain in two directions (labelled c in Fig. 6). The deformation of such architected materials is characterized by $\epsilon_1\neq 0$ and $\epsilon_2=\epsilon_3\approx 0$, resulting in $\delta=\|\epsilon\|$. Moreover, the results also reveal that there are a variety of structures capable of uniform biaxial expansion (or contraction), for which $\epsilon_2=\epsilon_3\neq 0$ and $\epsilon_1=0$ and $\|\epsilon\|=\delta/\sqrt{2}$. This deformation mode is exemplified by the design labelled d shown in Fig. 6 (Supplementary Video 4). Finally, we note that $\delta=\sqrt{3}\,\|\epsilon\|$ corresponds to uniform expansion (or contraction) characterized by $\epsilon_1=\epsilon_2=\epsilon_3$, and defines a boundary for possible combinations of δ and $\|\epsilon\|$. In fact, none of the designs considered here exhibits this type of deformation.

Discussion and conclusion

In this work we introduced a convenient and robust strategy for the design of reconfigurable architected materials, and explored the design space by considering structures based on the 28 uniform space-filling tessellations of polyhedra. Our study uncovered architected materials with a wide range of qualitatively different responses and degrees of freedom, but many more designs are made possible by using different assemblies of convex polyhedra as templates (including assemblies based on Johnson solids and irregular polyhedra, and assemblies that do not fill space), by considering different extrusion lengths, or by removing faces (instead of making them rigid before the extrusion step). Given these additional possibilities in the design of reconfigurable architected materials, we have made our numerical algorithm, implemented in Matlab, available for download as Supplementary Information, to be used and expanded upon by the community. Finally, we believe that, building on the results presented in this work, prismatic

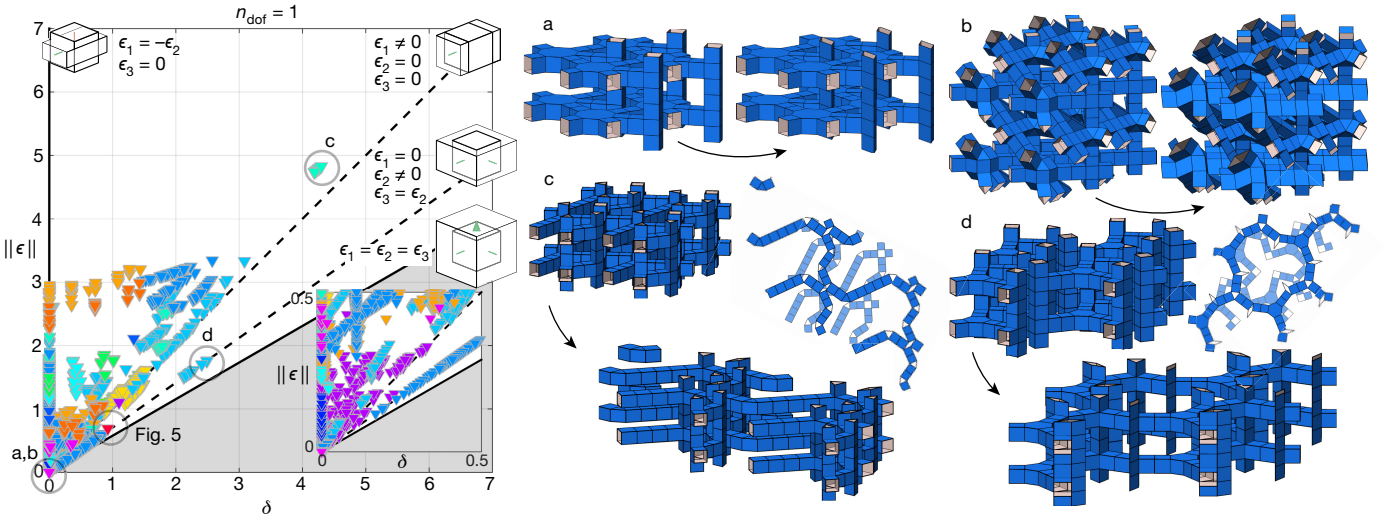

Figure 6 | Deformation modes of 3D prismatic architected materials with enhanced reconfigurability. Relation between the volumetric strain, δ, and the magnitude of the principal strains, $\|\epsilon\|$, for all the architected materials characterized by $n_{dof}=1$. The colour of the markers refers to the uniform tessellation that has been used as a template, as shown in Fig. 3. Structures a–d and the one in Fig. 5 are indicated by grey circles on the main panel. The solid and dashed lines and associated schematics and conditions on ϵ_1, ϵ_2 and ϵ_3 highlight how different choices of strains lead to different types of deformation (see text). Structures labelled a and b (based on tessellations 24 and 9, respectively) are characterized by $\delta=\|\epsilon\|=0$ and experience internal rearrangements that do not alter their macroscopic shape. The structure labelled c (based on tessellation 16) deforms only in one direction (that is, $\delta=4.21, \|\epsilon\|=4.76$), while the structure labelled d (based on tessellation 14) experiences uniform biaxial extension (or contraction) (that is, $\delta=2.45, \|\epsilon\|=1.73$). The grey shaded region corresponds to combinations of strains that do not permit deformation.

architected materials with specific properties may be efficiently identified by combining our numerical algorithm with stochastic optimization algorithms such as genetic algorithms. Such optimization algorithms could prove essential in the design of reconfigurable architected materials capable of handling changing environments or multiple tasks (that will probably lead to pareto optimal solutions).

To realize prismatic architected materials, in this study we used cardboard for the rigid faces and double-sided tape for the hinges. This fabrication process enables the realization of centimetre-scale prototypes (for our models we used $\overline{L} = 35$ mm) that closely match the conceptual origami-inspired mechanisms, but real-world applications depend on the ability to efficiently manufacture assemblies comprising a large number of unit cells at different length scales using different fabrication techniques. Taking advantage of recent developments in multi-material additive manufacturing, we also built the proposed architected materials using a stiff material (with Young's modulus $E \approx 1$ GPa) for the faces and a soft material ($E \approx 1$ MPa) for the hinges (see the 'Methods' section of Supplementary Information). Supplementary Video 5 shows 3D printed models for two designs based on assemblies of truncated octahedra (for both models we used $\overline{L} = 6$ mm). Although additional local deformation arises from the finite size of the flexible hinges, the 3D printed structures exhibit the same deformation modes predicted by our numerical analysis and observed in the cardboard prototypes. As such, recent advances in fabrication, including projection micro-stereolithography[7], two-photon lithography[8,32,33] and 'pop-up' strategies[34–40], open up exciting opportunities for miniaturization of the proposed architectures. Our strategy thus enables the design of a new class of reconfigurable systems across a wide range of length scales.

Data availability The Matlab model used to determine the mobility and deformation modes of the prismatic architected materials is provided in Supplementary Information. Other models and datasets generated during and/or analysed during the current study are available from the corresponding author on request.

Received 24 May; accepted 22 November 2016.

1. Reis, P. M., Jaeger, H. M. & van Hecke, M. Designer matter: a perspective. *Extreme Mech. Lett.* **5,** 25–29 (2015).
2. Sarrao, J. & Crabtree, G. Progress in mesoscale science. *MRS Bull.* **40,** 919–922 (2015).
3. Christensen, J., Kadic, M., Kraft, O. & Wegener, M. Vibrant times for mechanical metamaterials. *MRS Commun.* **5,** 453–462 (2015).
4. Pendry, J. B. Negative refraction makes a perfect lens. *Phys. Rev. Lett.* **85,** 3966–3969 (2000).
5. Smith, D. R., Pendry, J. B. & Wiltshire, M. C. K. Metamaterials and negative refractive index. *Science* **305,** 788–792 (2004).
6. Lakes, R. Foam structures with a negative Poisson's ratio. *Science* **235,** 1038–1040 (1987).
7. Zheng, X. *et al.* Ultralight, ultrastiff mechanical metamaterials. *Science* **344,** 1373–1377 (2014).
8. Meza, L. R., Das, S. & Greer, J. R. Strong, lightweight, and recoverable three-dimensional ceramic nanolattices. *Science* **345,** 1322–1326 (2014).
9. Ergin, T., Stenger, N., Brenner, P., Pendry, J. B. & Wegener, M. Three-dimensional invisibility cloak at optical wavelengths. *Science* **328,** 337–339 (2010).
10. Bückmann, T., Kadic, M., Schittny, R. & Wegener, M. Mechanical cloak design by direct lattice transformation. *Proc. Natl Acad. Sci. USA* **112,** 4930–4934 (2015).
11. Miura, K. *Method of Packaging and Deployment of Large Membranes in Space.* Report No. 618, https://repository.exst.jaxa.jp/dspace/handle/a-is/7293 (Institute of Space and Astronautical Science, 1985).
12. Wei, Z. Y., Guo, Z. V., Dudte, L., Liang, H. Y. & Mahadevan, L. Geometric mechanics of periodic pleated origami. *Phys. Rev. Lett.* **110,** 215501 (2013).
13. Schenk, M. & Guest, S. D. Geometry of miura-folded metamaterials. *Proc. Natl Acad. Sci. USA* **110,** 3276–3281 (2013).
14. Silverberg, J. L. *et al.* Using origami design principles to fold reprogrammable mechanical metamaterials. *Science* **345,** 647–650 (2014).
15. Lv, C., Krishnaraju, D., Konjevod, G., Yu, H. & Jiang, H. Origami based mechanical metamaterials. *Sci. Rep.* **4,** 5979 (2014).
16. Waitukaitis, S., Menaut, R., Chen, B. G. & van Hecke, M. Origami multistability: from single vertices to metasheets. *Phys. Rev. Lett.* **114,** 055503 (2015).
17. Dudte, L. H., Vouga, E., Tachi, T. & Mahadevan, L. Programming curvature using origami tessellations. *Nat. Mater.* **15,** 583–588 (2016).
18. Silverberg, J. L. *et al.* Origami structures with a critical transition to bistability arising from hidden degrees of freedom. *Nat. Mater.* **14,** 389–393 (2015).
19. Hawkes, E. *et al.* Programmable matter by folding. *Proc. Natl Acad. Sci. USA* **107,** 12441–12445 (2010).
20. Tachi, T. & Miura, K. Rigid-foldable cylinders and cells. *J. Int. Assoc. Shell Spat. Struct.* **53,** 217–226 (2012).
21. Filipov, E. T., Tachi, T. & Paulino, G. H. Origami tubes assembled into stiff, yet reconfigurable structures and metamaterials. *Proc. Natl Acad. Sci. USA* **112,** 12321–12326 (2015).
22. Cheung, K. C., Tachi, T., Calisch, S. & Miura, K. Origami interleaved tube cellular materials. *Smart Mater. Struct.* **23,** 094012 (2014).
23. Yasuda, H. & Yang, J. Re-entrant origami-based metamaterials with negative poisson's ratio and bistability. *Phys. Rev. Lett.* **114,** 185502 (2015).
24. Goldman, F. Using the snapology technique to teach convex polyhedra. In *Origami* Vol. 5 (eds Wang-Iverson, P., Lang, R. & Yim, M.) 99–110 (CRC Press, 2011).
25. Strobl, H. *Special Snapology* http://www.knotology.eu/PPP-Jena2010e/start.html (2010).
26. Overvelde, J. T. B. *et al.* A three-dimensional actuated origami-inspired transformable metamaterial with multiple degrees of freedom. *Nat. Commun.* **7,** 10929 (2016).
27. Felton, S., Tolley, M., Demaine, E., Rus, D. & Wood, R. A method for building self-folding machines. *Science* **345,** 644–646 (2014).
28. Andreini, A. Sulle reti di poliedri regolari e semiregolari e sulle corrispondenti reti correlative. *Mem. Soc. Ital. Sci.* **14,** 75–129 (1907).
29. Pearce, P. & Pearce, S. *Polyhedra Primer* (Nostrand Reinhold, 1978).
30. Grunbaum, B. Uniform tilings of 3-space. *Geombinatorics* **4,** 49–56 (1994).
31. Laliberté, T. & Gosselin, C. Construction, mobility analysis and synthesis of polyhedra with articulated faces. *J. Mech. Robot.* **6,** 011007 (2013).
32. Bauer, J., Hengsbach, S., Tesari, I., Schwaiger, R. & Kraft, O. High-strength cellular ceramic composites with 3D microarchitecture. *Proc. Natl Acad. Sci. USA* **111,** 2453–2458 (2014).
33. Meza, L. R. *et al.* Resilient 3D hierarchical architected metamaterials. *Proc. Natl Acad. Sci. USA* **112,** 11502–11507 (2015).
34. Leong, T. G. *et al.* Tetherless thermobiochemically actuated microgrippers. *Proc. Natl Acad. Sci. USA* **106,** 703–708 (2009).
35. Liu, Y., Boyles, J. K., Genzer, J. & Dickey, M. D. Self-folding of polymer sheets using local light absorption. *Soft Matter* **8,** 1764–1769 (2012).
36. Laflin, K. E., Morris, C. J., Muqeem, T. & Gracias, D. H. Laser triggered sequential folding of microstructures. *Appl. Phys. Lett.* **101,** 131901 (2012).
37. Shenoy, V. B. & Gracias, D. H. Self-folding thin-film materials: from nanopolyhedra to graphene origami. *MRS Bull.* **37,** 847–854 (2012).
38. Cho, J. H. *et al.* Nanoscale origami for 3D optics. *Small* **7,** 1943–1948 (2011).
39. Xu, S. *et al.* Assembly of micro/nanomaterials into complex, three-dimensional architectures by compressive buckling. *Science* **347,** 154–159 (2015).
40. Kim, J., Hanna, J. A., Byun, M., Santangelo, C. D. & Hayward, R. C. Designing responsive buckled surfaces by halftone gel lithography. *Science* **335,** 1201–1205 (2012).

Supplementary Information is available in the online version of the paper.

Acknowledgements This work was supported by the Materials Research Science and Engineering Center under NSF Award number DMR-1420570. K.B. also acknowledges support from the National Science Foundation (CMMI-1149456-CAREER). We thank M. Mixe and S. Shuham for assistance in the fabrication of the cardboard prototypes, and R. Wood for the use of his laboratory.

Author Contributions J.T.B.O., C.H. and K.B. proposed and designed the research; J.T.B.O. performed the numerical calculations; J.T.B.O., C.H. and J.C.W. designed and fabricated the models; J.T.B.O. performed the experiments; J.T.B.O. and K.B. wrote the paper.

Author Information Reprints and permissions information is available at www.nature.com/reprints. The authors declare no competing financial interests. Readers are welcome to comment on the online version of the paper. Correspondence and requests for materials should be addressed to K.B. (bertoldi@seas.harvard.edu).

Reviewer Information *Nature* thanks J. Paik, D. Pasini and the other anonymous reviewer(s) for their contribution to the peer review of this work.

doi:10.1038/nature20824

In the following, we first describe the fabrication approaches used to make cardboard prototypes and 3D printed prototypes. We next describe the numerical algorithms we implemented in Matlab (*i*) to predict the number of degrees of freedom and corresponding deformation modes of 3D prismatic architected materials with rigid faces; and (*ii*) to characterize the elastic response of 3D prismatic architected materials with deformable faces. Moreover, this document contains the supplemental figures and table.

METHODS

Fabrication of Cardboard Prototypes

Our cardboard prototypes were fabricated from two layers of cardboard with a thickness of 0.7 mm (13001-2506, Blick) and one layer of double-sided tape with a thickness of 0.07 mm (23205-1009, Blick), using a stepwise layering and laser cutting technique on a CO2 laser system (VLS 2.3, Universal Laser Systems). To fabricate each of the extruded polygons that together form the architected material, we started by cutting one of the cardboard sheets, after which we removed it from the laser system (steps 1-2 as shown in Supplementary Fig. 1). Using a different pattern, cutting slits were introduced in the second cardboard sheet (steps 3-5). The double-sided tape was bonded to the second cardboard sheet still in the laser system, to which the initially cut cardboard sheet was attached (steps 6-7). A third cutting step was then performed to finalize the different components (step 8), which were completely separated from the main sheet (step 9-10). The individual components were assembled to form the extruded architected material using the tape that was exposed during the cutting process (steps 11-15).

Fabrication of 3D Printed Prototypes

We furthermore manufactured prismatic architected materials using multi-material additive manufacturing (Connex500, Stratasys). We used a rigid material (VeroWhitePlus RGD835, Young's modulus $E \approx 1$ GPa) for the faces and a softer (TangoPlus FLX930, $E \approx 1$ MPa) for the hinges. The final structure was designed using a custom made Matlab script, which was based on extruded polyhedra with an edge length of $L^0 = 6$ mm and an average extrusion length of $\bar{L} = 6$ mm. Both the faces and hinges were given a thickness of $t = 1$ mm. Moreover, the size of the faces was reduced by $0.5 + 1.5|\theta|/\pi$ mm on each side to account for the finite size of the rounded hinges, θ being the initial angle of the hinges (Supplementary Fig. 2).

MODE ANALYSIS FOR 3D PRISMATIC ARCHITECTED MATERIALS WITH RIGID FACES

Here, we describe the algorithm that we implemented to predict the number of degrees of freedom and corresponding deformation modes of 3D prismatic architected materials. Focusing on an extruded unit cell comprising $2F$ rigid faces (F face pairs) connected by H hinges (i.e. torsional springs), we first determine the elastic and kinetic energy required to deform the structure. Then, we describe the constraints that we impose to ensure that the faces remain rigid and the unit cell deforms in a periodically repeated manner (i.e. we model the response of an infinitely large structure without considering boundary effects), after which we describe the eigenfrequency problem that we solve to find the characteristic deformation modes of the architected materials. Finally, we discuss the assumptions made in the numerical model.

Energy

Elastic Energy

Assuming that each hinge acts as a linear torsional spring of stiffness K^{h}, that no energy is required to maintain the hinges in their initial configuration and that the faces are rigid, the total elastic energy of the unit cell, E_{elastic},

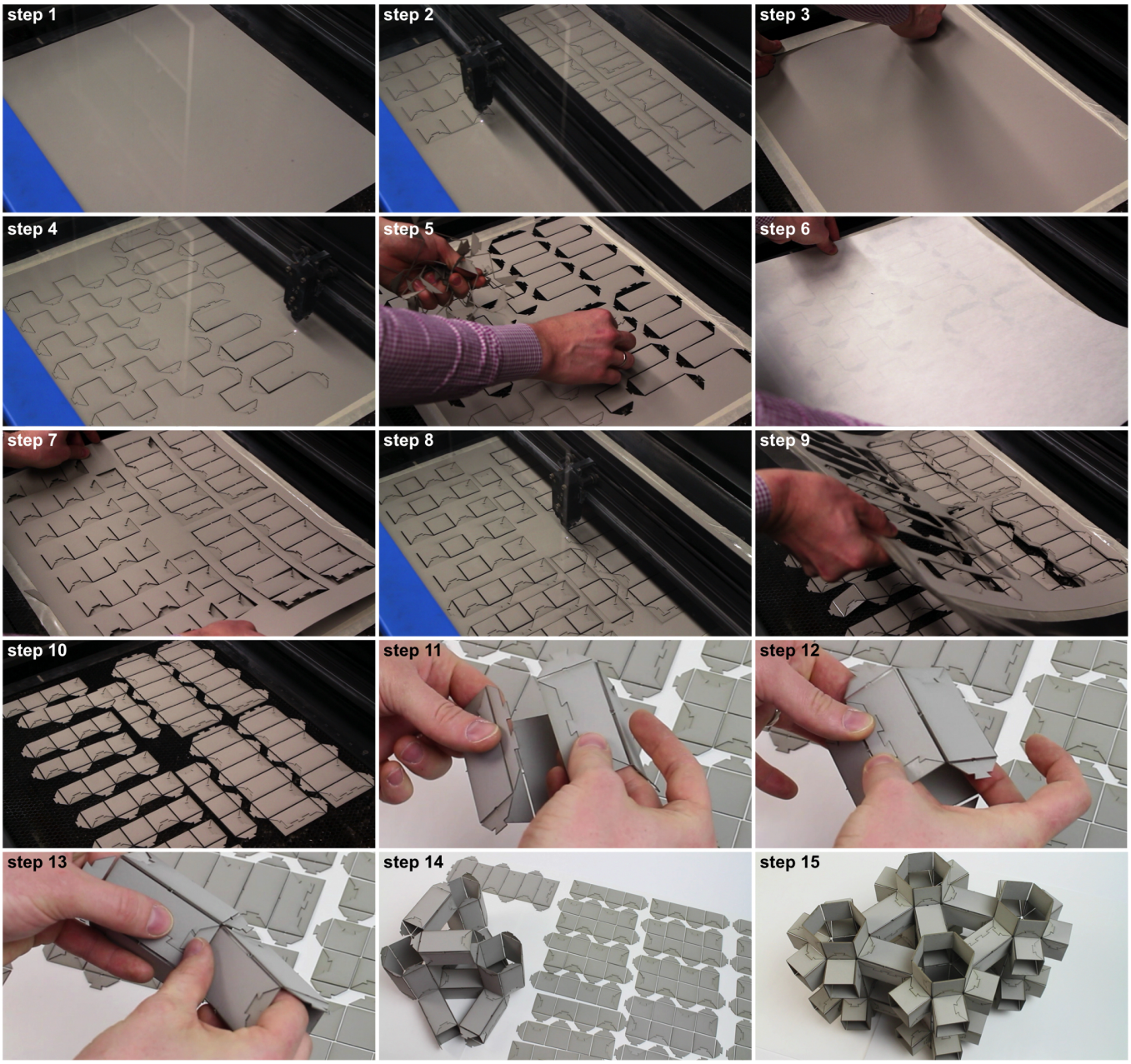

Supplementary Fig. 1: Fabrication of cardboard prototypes. Steps 1-10 show the cutting proces to fabricate flat three layer composites of cardboard and double-sided tape, and steps 11-16 depict the assembly process using the fabricated fabricated pieces.

is given by

$$E_{\text{elastic}} = E_{\text{hinge}} = \sum_{i=1}^{H} \frac{1}{2} K_i^{\text{h}} d\theta_i^2 = \frac{1}{2} d\boldsymbol{\theta}^T \mathbf{K}_{\text{h}} d\boldsymbol{\theta}, \tag{1}$$

where $d\theta_i$ denotes the change in angle for the i-th hinge, $d\boldsymbol{\theta} = [d\theta_1, d\theta_2, \ldots, d\theta_H]^T$, and $\mathbf{K}_{\text{h}} = \text{diag}(K_1^{\text{h}}, K_2^{\text{h}}, ..., K_H^{\text{h}})$. Note that $d\theta_i$ can be expressed in terms of the displacement of the V vertices (corner points of the faces) as

$$d\theta_i = \sum_{v=1}^{V} \left(\frac{\partial \theta_i}{\partial x_{1,v}} dx_{1,v} + \frac{\partial \theta_i}{\partial x_{2,v}} dx_{2,v} + \frac{\partial \theta_i}{\partial x_{3,v}} dx_{3,v} \right), \tag{2}$$

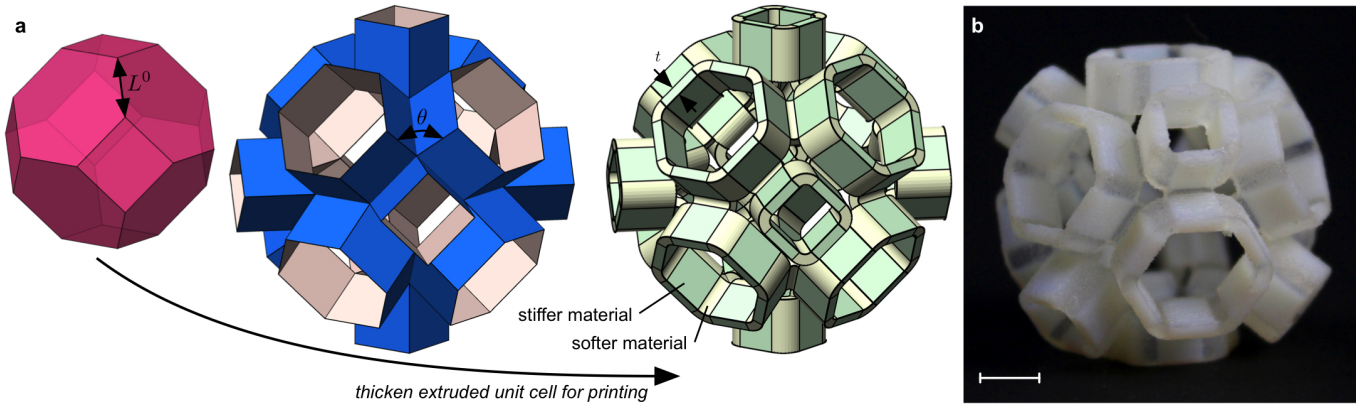

Supplementary Fig. 2: Fabrication of 3D printed prototypes. (a) Multi-material design based on a polyhedron template. Here, L^0 depicts the edge size, θ the angle between faces, and t the thickness of the faces. (b) 3D printed prototype using stiff materials for the faces, and soft material for the hinges. (scale bar 6 mm)

where $dx_{1,v}$, $dx_{2,v}$ and $dx_{3,v}$ denote the displacement components of the v-th vertex with initial coordinates $x_{1,v}$, $x_{2,v}$ and $x_{3,v}$. Substitution of Eq. (2) into Eq. (1) yields

$$E_{\text{hinge}} = \frac{1}{2}\mathbf{u}^T\mathbf{J}_{\text{h}}^T\mathbf{K}_{\text{h}}\mathbf{J}_{\text{h}}\mathbf{u}, \tag{3}$$

in which $\mathbf{J}_{\text{h}}$ is the Jacobian matrix with entries

$$J_{\text{h}[i,\,3(v-1)+j]} = \frac{\partial\theta_i}{\partial x_{j,v}}, \quad j = 1,2,3 \text{ and } v = 1,...,V, \tag{4}$$

and $\mathbf{u} = [dx_{1,1}, dx_{2,1}, dx_{3,1}, \ldots, dx_{1,V}, dx_{2,V}, dx_{3,V}]^T$.

Since the angle of the i-th hinge, which connects two faces with unit normals $\mathbf{n}_{\text{a}}$ and $\mathbf{n}_{\text{b}}$ and rotates around the axis pointing in the direction $\mathbf{a}_{\text{h}}$, is given by

$$\theta_i = \tan^{-1}\left(\frac{\mathbf{a}_{\text{h}}\cdot(\mathbf{n}_{\text{a}}\times\mathbf{n}_{\text{b}})}{\mathbf{n}_{\text{a}}\cdot\mathbf{n}_{\text{b}}}\right), \tag{5}$$

it follows that

$$\frac{\partial\theta_i}{\partial x_{j,v}} = \frac{\frac{\partial y}{\partial x_{j,v}}z - y\frac{\partial z}{\partial x_{j,v}}}{y^2+z^2}, \tag{6}$$

in which we have used $y = \mathbf{a}_{\text{h}}\cdot(\mathbf{n}_{\text{a}}\times\mathbf{n}_{\text{b}})$ and $z = \mathbf{n}_{\text{a}}\cdot\mathbf{n}_{\text{b}}$. The derivatives can then be found according to

$$\frac{\partial y}{\partial x_{j,v}} = \frac{\partial\mathbf{a}_{\text{h}}}{\partial x_{j,v}}\cdot(\mathbf{n}_{\text{a}}\times\mathbf{n}_{\text{b}}) + \mathbf{a}_{\text{h}}\cdot\left(\frac{\partial\mathbf{n}_{\text{a}}}{\partial x_{j,v}}\times\mathbf{n}_{\text{b}} + \mathbf{n}_{\text{a}}\times\frac{\partial\mathbf{n}_{\text{b}}}{\partial x_{j,v}}\right), \tag{7}$$

and

$$\frac{\partial z}{\partial x_{j,v}} = \frac{\partial\mathbf{n}_{\text{a}}}{\partial x_{j,v}}\cdot\mathbf{n}_{\text{b}} + \mathbf{n}_{\text{a}}\cdot\frac{\partial\mathbf{n}_{\text{b}}}{\partial x_{j,v}} \tag{8}$$

Finally, since the unit normal to any of the faces, $\mathbf{n}$, can be calculated as

$$\mathbf{n} = \frac{\mathbf{v}_1\times\mathbf{v}_2}{\sqrt{|\mathbf{v}_1|^2|\mathbf{v}_2|^2 - (\mathbf{v}_1\cdot\mathbf{v}_2)^2}}, \tag{9}$$

where $\mathbf{v}_1$ and $\mathbf{v}_2$ are two non-parallel vectors lying on the face (Supplementary Fig. 3), the derivatives of $\mathbf{n}$ in Eqs. (7) and (8) are given by

$$\frac{\partial\mathbf{n}}{\partial x_{j,v}} = \frac{\left(\frac{\partial\mathbf{v}_1}{\partial x_{j,v}}\times\mathbf{v}_2 + \mathbf{v}_1\times\frac{\partial\mathbf{v}_2}{\partial x_{j,v}}\right)c - (\mathbf{v}_1\times\mathbf{v}_2)\frac{\partial c}{\partial x_{j,v}}}{c^2}, \tag{10}$$

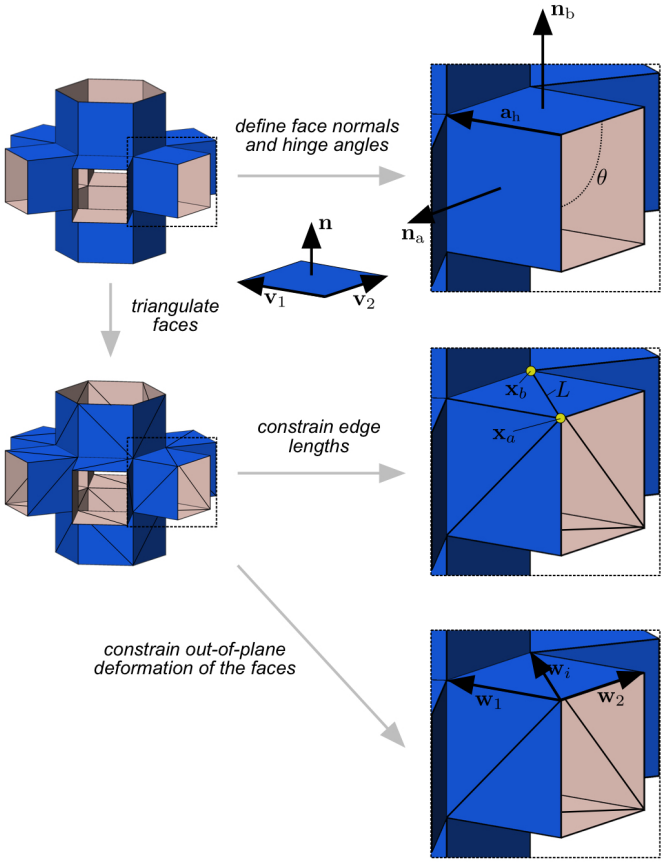

Supplementary Fig. 3: Schematic of the extruded unit cell.

in which

$$c = \sqrt{|\mathbf{v}_1|^2|\mathbf{v}_2|^2 - (\mathbf{v}_1 \cdot \mathbf{v}_2)^2}, \tag{11}$$

and

$$\frac{\partial c}{\partial x_{j,v}} = \frac{1}{c}\left[\left(\frac{\partial \mathbf{v}_1}{\partial x_{j,v}} \cdot \mathbf{v}_1\right)|\mathbf{v}_2|^2 + |\mathbf{v}_1|^2\left(\frac{\partial \mathbf{v}_2}{\partial x_{j,v}} \cdot \mathbf{v}_2\right) - (\mathbf{v}_1 \cdot \mathbf{v}_2)\left(\frac{\partial \mathbf{v}_1}{\partial x_{j,v}} \cdot \mathbf{v}_2 + \mathbf{v}_1 \cdot \frac{\partial \mathbf{v}_2}{\partial x_{j,v}}\right)\right]. \tag{12}$$

Note that $\partial \mathbf{n}/\partial x_{j,v} = 0$ for vertices not belonging to the face with normal $\mathbf{n}$.

Kinetic Energy

Next, we determine the kinetic energy, E_{kinetic}, associated with the displacements of the vertices of the unit cell

$$E_{\text{kinetic}} = \frac{1}{2}\sum_{v=1}^{V} M_v \left(\frac{\partial x_{1,v}}{\partial t} + \frac{\partial x_{2,v}}{\partial t} + \frac{\partial x_{3,v}}{\partial t}\right)^2 = \frac{1}{2}\dot{\mathbf{u}}^T \mathbf{M} \dot{\mathbf{u}}, \tag{13}$$

where $\dot{\mathbf{u}} = \partial \mathbf{u}/\partial t$, M_v is the mass assigned to the v-th vertex and $\mathbf{M}$ is the $3V \times 3V$ diagonal mass matrix $\text{diag}(M_1, M_1, M_1, \ldots, M_V, M_V, M_V)$. Note that each face to which the v-th vertex belongs contributes a mass M/N to the vertex, where M is the mass of the face (which we take equal to the area by assuming a unit thickness and density), and N is the number of vertices of the face.

Constraints

Rigidity of the Faces

To ensure that all the faces are rigid and do not deform, we triangulate them (Supplementary Fig. 3) and impose that the length of each edge of the triangulation remains constant,

$$(\mathbf{x}_\mathrm{a} - \mathbf{x}_\mathrm{b}) \cdot (\mathbf{x}_\mathrm{a} - \mathbf{x}_\mathrm{b}) = L^2, \tag{14}$$

where $\mathbf{x}_\mathrm{a}$ and $\mathbf{x}_\mathrm{b}$ are the two vertices connected by the edge, which has initial length L. We then linearize Eq. (14) to obtain an expressions for each constraint that depends explicitly on the displacements of the two vertices

$$(\mathbf{x}_\mathrm{a} - \mathbf{x}_\mathrm{b}) \cdot (\mathbf{u}_\mathrm{a} - \mathbf{u}_\mathrm{b}) = 0, \tag{15}$$

in which $\mathbf{u}_\mathrm{a} = [dx_{1,\mathrm{a}}, dx_{2,\mathrm{a}}, dx_{3,\mathrm{a}}]$ and $\mathbf{u}_\mathrm{b} = [dx_{1,\mathrm{b}}, dx_{2,\mathrm{b}}, dx_{3,\mathrm{b}}]$.

Furthermore, we also ensure that all the faces remain flat (i.e. each face can undergo rigid body translation and rotations, but cannot bend). To this end, we impose that all vertices of each face remain on the same plane spanned by the two vectors $\mathbf{w}_1$ and $\mathbf{w}_2$ (Supplementary Fig. 3) [41],

$$\mathbf{w}_i \cdot (\mathbf{w}_1 \times \mathbf{w}_2) = 0, \quad \text{for} \quad i = 3, ..., V_f - 1, \tag{16}$$

in which V_f is the number of vertices of the face. Note that this constraint is automatically satisfied for faces that only connect three vertices. We again linearize the constraints to obtain

$$\mathbf{u}_1 \cdot (\mathbf{w}_i \times \mathbf{w}_2) + \mathbf{u}_2 \cdot (\mathbf{w}_2 \times \mathbf{w}_i) + \mathbf{u}_3 \cdot (\mathbf{w}_i \times \mathbf{w}_1) + \mathbf{u}_i \cdot (\mathbf{w}_1 \times \mathbf{w}_2) = 0, \quad \text{for} \quad i = 3, ..., V_f - 1. \tag{17}$$

Finally, we note that the constraints of Eqs. (15) and (17) are only valid for small displacements, since the constraints are linearized around the initial coordinates of the vertices.

Periodic Boundary Conditions

For the infinitely large periodic prismatic architected materials considered here, it is sufficient to focus on a unit cell that consists of a few extruded polyhedra and covers the entire assembly when translated by the three lattice vectors $\mathbf{l}_i$ ($i = 1, 2, 3$). To ensure that the extruded unit cell deforms in a periodically repeated manner we constrain the deformation of each periodically located vertex pair on its boundary as

$$\mathbf{u}_\mathrm{b} - \mathbf{u}_\mathrm{a} = \sum_{i=1}^{3} \alpha_i d\mathbf{l}_i, \tag{18}$$

where $\mathbf{u}_\mathrm{a}$ and $\mathbf{u}_\mathrm{b}$ are the displacements of the two periodically located vertices, $d\mathbf{l}_i$ denotes the deformation of the lattice vectors, and

$$\mathbf{x}_\mathrm{b} - \mathbf{x}_\mathrm{a} = \sum_{i=1}^{3} \alpha_i \mathbf{l}_i, \tag{19}$$

with $\alpha_i \in \{-1, 0, 1\}$. In our implementation we treat $d\mathbf{l}_i$ as additional degrees of freedom, which we include in Eqs. (3) and (13) as

$$E_\mathrm{elastic} = \frac{1}{2} \begin{bmatrix} \mathbf{u} \\ d\mathbf{l} \end{bmatrix}^T \begin{bmatrix} \mathbf{J}_\mathrm{h} & \mathbf{0} \end{bmatrix}^T \mathbf{K}_\mathrm{h} \begin{bmatrix} \mathbf{J}_\mathrm{h} & \mathbf{0} \end{bmatrix} \begin{bmatrix} \mathbf{u} \\ d\mathbf{l} \end{bmatrix}, \tag{20}$$

and

$$E_\mathrm{kinetic} = \frac{1}{2} \begin{bmatrix} \dot{\mathbf{u}} \\ d\dot{\mathbf{l}} \end{bmatrix}^T \begin{bmatrix} \mathbf{M} & \mathbf{0} \\ \mathbf{0} & \mathbf{0} \end{bmatrix} \begin{bmatrix} \dot{\mathbf{u}} \\ d\dot{\mathbf{l}} \end{bmatrix}, \tag{21}$$

in which $d\mathbf{l} = [d\mathbf{l}_1^T, d\mathbf{l}_2^T, d\mathbf{l}_3^T]^T$ and $d\dot{\mathbf{l}} = \partial d\mathbf{l}/dt$.

Master-slave Elimination

To enforce the constraints given by Eqs. (15), (17) and (18), we adopt the master-slave elimination method [42]. We start by rewriting all the constraints in matrix form as

$$\mathbf{A}\begin{bmatrix}\mathbf{u}\\ d\mathbf{l}\end{bmatrix} = \mathbf{0}, \tag{22}$$

where each row of $\mathbf{A}$ represents one constraint. Next, we rewrite $\mathbf{A}$ in its reduced row echelon form, $\mathbf{A}_{\text{rref}}$. The dependent constraints correspond to rows of all zeros in $\mathbf{A}_{\text{rref}}$ and are therefore automatically satisfied. Moreover, all the columns of $\mathbf{A}_{\text{rref}}$ with a single entry correspond to the slave degree of freedom, $\mathbf{d}_{\text{s}}$, while the remaining degrees of freedom are referred to as the master degree of freedom, $\mathbf{d}_{\text{m}}$. We then rewrite Eq. (22) as

$$\begin{bmatrix}\mathbf{I} & \mathbf{B}_{\text{rref}}\end{bmatrix}\begin{bmatrix}\mathbf{d}_{\text{s}}\\ \mathbf{d}_{\text{m}}\end{bmatrix} = \mathbf{0}, \tag{23}$$

where $\mathbf{I}$ is the identity matrix and $\mathbf{B}_{\text{rref}}$ comprise the columns of $\mathbf{A}_{\text{rref}}$ that correspond to the master degrees of freedom. It follows from Eq. (23) that

$$\mathbf{d}_{\text{s}} = -\mathbf{B}_{\text{rref}}\mathbf{d}_{\text{m}}, \tag{24}$$

so that

$$\begin{bmatrix}\mathbf{d}_{\text{s}}\\ \mathbf{d}_{\text{m}}\end{bmatrix} = \begin{bmatrix}-\mathbf{B}_{\text{rref}}\\ \mathbf{I}\end{bmatrix}\mathbf{d}_{\text{m}}. \tag{25}$$

Finally, since the vectors $[\mathbf{d}_{\text{s}}^T, \mathbf{d}_{\text{m}}^T]^T$ and $[\mathbf{u}^T, d\mathbf{l}^T]^T$ contain exactly the same degrees of freedom arranged in a different order, we rearrange the rows of the matrix $[\mathbf{B}_{\text{rref}}, \mathbf{I}]^T$ in Eq. (25) to obtain

$$\begin{bmatrix}\mathbf{u}\\ d\mathbf{l}\end{bmatrix} = \mathbf{T}\mathbf{d}_{\text{m}}, \tag{26}$$

where $\mathbf{T}$ is a transformation matrix.

Using Eq. (26), the elastic and kinetic energies from Eqs. (20) and (21) can be rewritten as

$$E_{\text{elastic}} = \mathbf{d}_{\text{m}}^T\mathbf{T}^T\begin{bmatrix}\mathbf{J}_{\text{h}} & \mathbf{0}\end{bmatrix}^T\mathbf{K}_{\text{h}}\begin{bmatrix}\mathbf{J}_{\text{h}} & \mathbf{0}\end{bmatrix}\mathbf{T}\mathbf{d}_{\text{m}}, \tag{27}$$

and

$$E_{\text{kinetic}} = \dot{\mathbf{d}}_{\text{m}}^T\mathbf{T}^T\begin{bmatrix}\mathbf{M} & \mathbf{0}\\ \mathbf{0} & \mathbf{0}\end{bmatrix}\mathbf{T}\dot{\mathbf{d}}_{\text{m}}. \tag{28}$$

Mode Analysis

The equations of motion for the extruded unit cell are derived using Lagrange's equations

$$\frac{\partial}{\partial t}\left(\frac{\partial E_{\text{potential}}}{\partial \dot{\mathbf{u}}}\right) - \frac{\partial E_{\text{potential}}}{\partial \mathbf{u}} = \mathbf{0}, \tag{29}$$

where $E_{\text{potential}} = E_{\text{elastic}} - E_{\text{kinetic}}$. Substitution of Eqs. (27) and (28) into Eq. (29) yields

$$\mathbf{T}^T\begin{bmatrix}\mathbf{M} & \mathbf{0}\\ \mathbf{0} & \mathbf{0}\end{bmatrix}\mathbf{T}\ddot{\mathbf{d}}_{\text{m}} - \mathbf{T}^T\begin{bmatrix}\mathbf{J}_{\text{h}} & \mathbf{0}\end{bmatrix}^T\mathbf{K}_{\text{h}}\begin{bmatrix}\mathbf{J}_{\text{h}} & \mathbf{0}\end{bmatrix}\mathbf{T}\mathbf{d}_{\text{m}} = \mathbf{0}, \tag{30}$$

in which we assumed that $\mathbf{T}$, $\mathbf{M}$, $\mathbf{J}_{\text{h}}$ and $\mathbf{K}_{\text{h}}$ do not depend on the displacement and do not change in time. Next, we assume the solution to have the form

$$\mathbf{d}_{\text{m}} = \mathbf{a}_{\text{m}}\sin(\omega t + \beta), \tag{31}$$

and substitute into Eq. (29) to obtain the eigenproblem

$$\tilde{\mathbf{M}}^{-1}\tilde{\mathbf{K}}\mathbf{a}_{\mathrm{m}} = \omega^2\mathbf{a}_{\mathrm{m}}, \tag{32}$$

in which

$$\tilde{\mathbf{M}} = \left(\mathbf{T}^T\begin{bmatrix}\mathbf{M} & \mathbf{0}\\ \mathbf{0} & \mathbf{0}\end{bmatrix}\mathbf{T}\right), \tag{33}$$

$$\tilde{\mathbf{K}} = \mathbf{T}^T\begin{bmatrix}\mathbf{J}_{\mathrm{h}} & \mathbf{0}\end{bmatrix}^T\mathbf{K}_{\mathrm{h}}\begin{bmatrix}\mathbf{J}_{\mathrm{h}} & \mathbf{0}\end{bmatrix}\mathbf{T}. \tag{34}$$

Moreover, ω is an eigenfrequency of the system and $\mathbf{a}_{\mathrm{m}}$ is the corresponding mode. Finally, the displacements of all the vertices associated to each mode are obtained from Eq. (26) as

$$\begin{bmatrix}\mathbf{u}\\ d\mathbf{l}\end{bmatrix} = \mathbf{T}\mathbf{a}_{\mathrm{m}}\sin(\omega t+\beta). \tag{35}$$

Characterizing the deformation modes

To characterize the macroscopic deformation associated to each prismatic material, we determine the macroscopic infinitesimal strain tensor for each of the computed modes as

$$\bar{\mathbf{e}} = \frac{1}{2}\left(\overline{\mathbf{H}} + \overline{\mathbf{H}}^T\right), \tag{36}$$

where $\overline{\mathbf{H}}$ is the macroscopic displacement gradient, which can be determined from the infinitesimal deformation of the three lattice vectors, $d\mathbf{l}_i$, by solving the following set of equations

$$d\mathbf{l}_i = \overline{\mathbf{H}}\mathbf{l}_i, \quad \text{for} \quad i = 1,2,3. \tag{37}$$

Note that we normalized $d\mathbf{l}_i$ by the maximum change in angle between connected faces. To characterize the type of macroscopic deformation associated to each mode we introduce the volumetric strain

$$\delta = \sum_{j=1}^{3}\epsilon_j, \tag{38}$$

where ϵ_j are the principal strains, which can be determined by solving $\left(\bar{\mathbf{e}} - \epsilon_j\mathbf{I}\right)\mathbf{v}_j = \mathbf{0}$, $\mathbf{v}_j$ being the principal directions.

Discussion

While our numerical analysis proved essential in the exploration of the design space for prismatic architected materials, it is important to note that the algorithm is only valid for small rotations. However, we found that the numerical results still provide valuable insights into the large deformations typically experienced by the structures, as demonstrated by the excellent agreement with the experiments. Moreover, in our model we assumed that the deformation of the architected material can be fully captured by an extruded unit cell to which periodic boundary conditions are applied, thus neglecting boundary effects. Although in our experiments we observed additional modes that arise from the reduced connectivity of the unit cells near the boundaries (Supplementary Fig. 4), we do not expect them to significantly influence the behavior of the bulk material as they are confined to the outer surfaces. These assumptions significantly reduced computation time and also removed the need for applying specific boundary conditions, allowing us to model and compare many different systems.

STIFFNESS OF 3D PRISMATIC ARCHITECTED MATERIALS WITH DEFORMABLE FACES

While in the analysis used to characterize the reconfigurability of the structures we assumed the faces to be rigid, we now account also for their deformability by introducing a set of springs. More specifically, for each rectangular

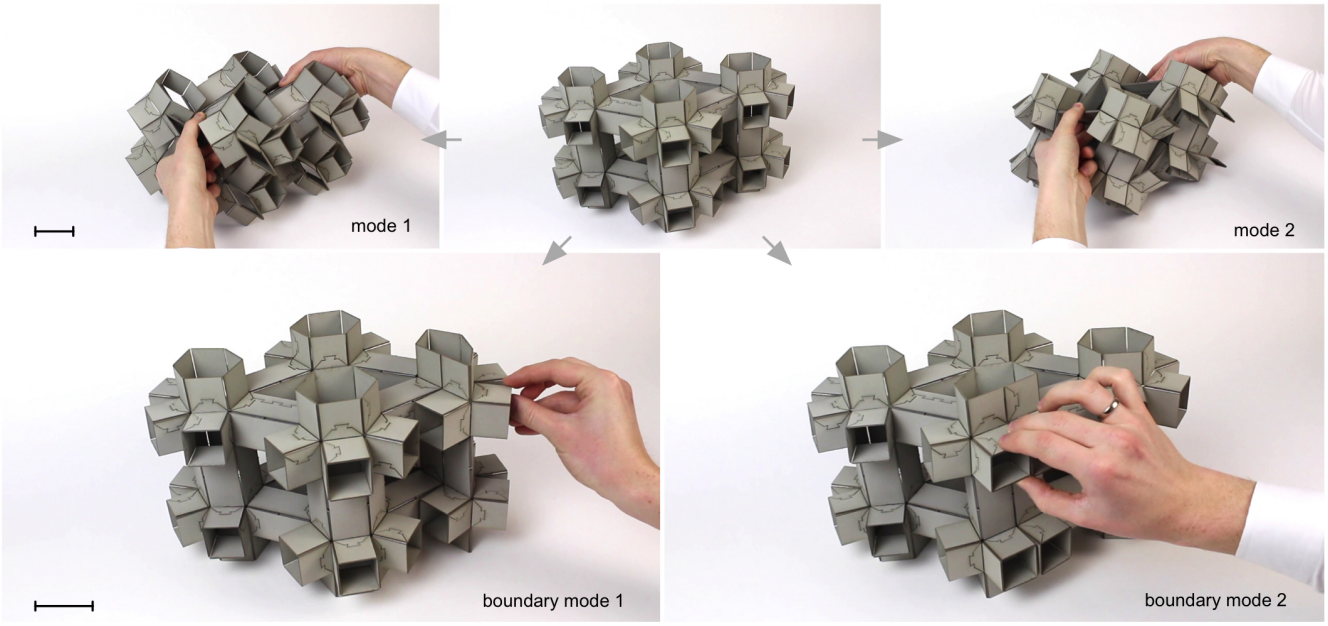

Supplementary Fig. 4: Deformation modes of a finite-size prototype of the architected material based on the space-filling assembly of hexagonal prisms (#26). Besides the two bulk modes predicted by our numerical simulations, we also observe 6 boundary modes (of which 2 are shown) that arise from the reduced connectivity of the unit cells near the boundaries (scale bar 5 cm).

face we used four linear springs placed along the perimeter to capture its stretching, two linear springs placed along the diagonal to capture its shearing, and a linear torsional spring placed along an arbitrary diagonal to capture its bending [43–45] (Supplementary Fig. 5). Therefore, the elastic energy required to deform an extruded unit cell is given by

$$E_{\text{elastic}} = E_{\text{hinge}} + E_{\text{face}}^{\text{stretch}} + E_{\text{face}}^{\text{shear}} + E_{\text{face}}^{\text{bend}}, \tag{39}$$

where E_{hinge} is the elastic energy as defined in in Eq. (1), and $E_{\text{face}}^{\text{stretch}}$, $E_{\text{face}}^{\text{shear}}$ and $E_{\text{face}}^{\text{bend}}$ denote the contribution to the elastic energy of the unit cell due to stretching, shearing and bending of the faces. Focusing on unit cells comprising $2F$ faces, the energy required to stretch the faces can be determined from the extension of their edges as

$$E_{\text{face}}^{\text{stretch}} = \sum_{i=1}^{8F} \frac{1}{2} K_i^{\text{st}} (de_i^{\text{st}})^2 = \frac{1}{2} d\mathbf{e}_{\text{st}}^T \mathbf{K}_{\text{st}} d\mathbf{e}_{\text{st}}, \tag{40}$$

where K_i^{st} and de_i^{st} denote the stiffness and change in length of the i-th edge, $d\mathbf{e}_{\text{st}} = [de_1^{\text{st}}, de_2^{\text{st}}, \ldots, de_{8F}^{\text{st}}]^T$, and $\mathbf{K}_{\text{st}} = \text{diag}(K_1^{\text{st}}, K_2^{\text{st}}, ..., K_{8F}^{\text{st}})$. Following the same approach used for E_{hinge} (Eqs. (2)-(4)), we rewrite $E_{\text{face}}^{\text{stretch}}$ in terms of the displacement of the V vertices. We first note that

$$de_i^{\text{st}} = \sum_{v=1}^{V} \left(\frac{\partial e_i^{\text{st}}}{\partial x_{1,v}} dx_{1,v} + \frac{\partial e_i^{\text{st}}}{\partial x_{2,v}} dx_{2,v} + \frac{\partial e_i^{\text{st}}}{\partial x_{3,v}} dx_{3,v} \right). \tag{41}$$

Next, we substitute Eq. (41) into Eq. (40) and obtain

$$E_{\text{face}}^{\text{stretch}} = \frac{1}{2} \mathbf{u}^T \mathbf{J}_{\text{st}}^T \mathbf{K}_{\text{st}} \mathbf{J}_{\text{st}} \mathbf{u}, \tag{42}$$

in which $\mathbf{J}_{\text{st}}$ is the compatibility matrix with entries

$$J_{\text{st}\,[i,\,3(v-1)+j]} = \frac{\partial e_i^{\text{st}}}{\partial x_{j,v}}, \; j = 1, 2, 3 \text{ and } i = 1, ..., 8F. \tag{43}$$

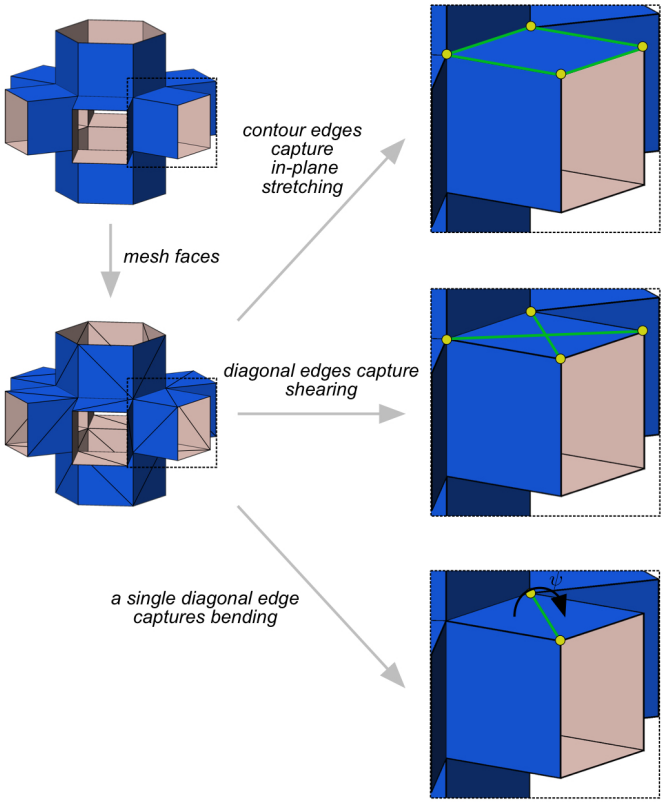

Supplementary Fig. 5: Schematic of the extruded unit cell indicating elements used to model the deformation of the faces.

Since shearing of faces is also modeled using springs (placed along the diagonals of the face), following the same procedure used for $E_{\text{face}}^{\text{stretch}}$ (Eqs. (40)-(43)), $E_{\text{face}}^{\text{shear}}$ can be determined as

$$E_{\text{face}}^{\text{shear}} = \frac{1}{2}\mathbf{u}^T\mathbf{J}_{\text{sh}}^T\mathbf{K}_{\text{sh}}\mathbf{J}_{\text{sh}}\mathbf{u}, \tag{44}$$

where $\mathbf{K}_{\text{sh}} = \text{diag}(K_1^{\text{sh}}, K_2^{\text{sh}}, ..., K_{4F}^{\text{sh}})$ (K_i^{sh} denoting the stiffness of the i-th diagonal spring introduced to capture shearing) and

$$J_{\text{sh}\,[i,\,3(v-1)+j]} = \frac{\partial e_i^{\text{sh}}}{\partial x_{j,v}},\ j = 1, 2, 3 \text{ and } i = 1, ..., 4F. \tag{45}$$

Finally, the energy associated to bending of the faces, $E_{\text{face}}^{\text{bend}}$, can be determined following the procedure used to determine E_{hinge} (Eq. (1)-(12)), yielding

$$E_{\text{face}}^{\text{bend}} = \frac{1}{2}\mathbf{u}^T\mathbf{J}_{\text{b}}^T\mathbf{K}_{\text{b}}\mathbf{J}_{\text{b}}\mathbf{u}. \tag{46}$$

where $\mathbf{K}_{\text{b}} = \text{diag}(K_1^{\text{b}}, K_2^{\text{b}}, ..., K_{2F}^{\text{b}})$ (K_i^{b} denoting the stiffness of the i-th torsional spring placed on the diagonal to capture shearing) and

$$J_{\text{b}\,[i,\,3(v-1)+j]} = \frac{\partial \psi_i}{\partial x_{j,v}},\ j = 1, 2, 3 \text{ and } i = 1, ..., 2F, \tag{47}$$

ψ being the angle between the two triangulated faces separated by the diagonal on which the torsional spring is placed (Supplementary Fig. 5).

Spring Stiffnesses

We assume that the faces are made from a material with Young's modulus E and Poisson's ratio $\nu = 1/3$, and their thickness t is chosen so that $t/\bar{L} = 0.01$ ($\bar{L}$ being the average extrusion length). For such systems the stiffnesses of

the springs introduced in our model can be determined as [45]

$$K^{\mathrm{st}} = \frac{Et}{2L^2}\frac{L^2-\nu L_\perp^2}{1-\nu^2}, \tag{48}$$

$$K^{\mathrm{sh}} = \frac{Et}{2LL_{\mathrm{H}}L_{\mathrm{W}}}\frac{\nu(L_{\mathrm{H}}^2+L_{\mathrm{W}}^2)^{3/2}}{1-\nu^2}, \tag{49}$$

$$K^{\mathrm{b}} = C_{\mathrm{b}}\frac{Et^3}{12(1-\nu^2)}\left(\frac{L}{t}\right)^{1/3} \tag{50}$$

in which L is the length of the edge on which the spring is placed, $L_\perp$ is the length of the edge perpendicular to that on which the spring is placed, L_{W} and L_{H} are the width and the height of the face, and $C_{\mathrm{b}} = 0.441$. Moreover, while in our experiments we used hinges that can bend more easily than the faces, here we consider the extreme case for which the bendability of the hinges is similar to that of the faces and use

$$K^{\mathrm{h}} = C_{\mathrm{b}}\frac{ELt^3}{24(1-\nu^2)}\left(\frac{1}{t}\right)^{1/3}. \tag{51}$$

Periodic boundary conditions

Next, we apply periodic boundary conditions to the unit cell and express them in terms of the macroscopic displacement gradient $\overline{\mathbf{H}}$. To ensure that the extruded unit cell deforms in a periodically repeated manner under applied loading we update Eq. (18) as

$$\mathbf{u}_{\mathrm{b}} - \mathbf{u}_{\mathrm{a}} = \sum_{i=1}^{3}\alpha_i\overline{\mathbf{H}}\mathbf{l}_i. \tag{52}$$

Furthermore, we also introduce three fictitious nodes, (v_1, v_2, v_3), to conveniently apply $\overline{\mathbf{H}}$ to the unit cell [46]. The displacement components of three fictitious nodes are assigned to be the components of $\overline{\mathbf{H}}$. Virtual work is then used to determine the macroscopic stress tensor as

$$\overline{s}_{ij} = \frac{1}{V_0}r_j^{v_i} \tag{53}$$

where V_0 is the initial volume occupied by the extruded unit cell and $\mathbf{r}^{v_i}$ is the "reaction force" corresponding to the assigned "displacement components" of the fictitious nodes v_i.

The periodic boundary conditions specified by Eq. (52) are then enforced using the master-slave elimination method. Following the procedure detailed in Eqs. (22)-(28) for E_{hinge}, we obtain

$$E_{\mathrm{face}}^{\mathrm{stretch}} = \mathbf{d}_{\mathrm{m}}^T\mathbf{T}^T\begin{bmatrix}\mathbf{J}_{\mathrm{st}} & \mathbf{0}\end{bmatrix}^T\mathbf{K}_{\mathrm{st}}\begin{bmatrix}\mathbf{J}_{\mathrm{st}} & \mathbf{0}\end{bmatrix}\mathbf{T}\mathbf{d}_{\mathrm{m}}, \tag{54}$$

$$E_{\mathrm{face}}^{\mathrm{shear}} = \mathbf{d}_{\mathrm{m}}^T\mathbf{T}^T\begin{bmatrix}\mathbf{J}_{\mathrm{sh}} & \mathbf{0}\end{bmatrix}^T\mathbf{K}_{\mathrm{sh}}\begin{bmatrix}\mathbf{J}_{\mathrm{sh}} & \mathbf{0}\end{bmatrix}\mathbf{T}\mathbf{d}_{\mathrm{m}}, \tag{55}$$

$$E_{\mathrm{face}}^{\mathrm{bend}} = \mathbf{d}_{\mathrm{m}}^T\mathbf{T}^T\begin{bmatrix}\mathbf{J}_{\mathrm{b}} & \mathbf{0}\end{bmatrix}^T\mathbf{K}_{\mathrm{b}}\begin{bmatrix}\mathbf{J}_{\mathrm{b}} & \mathbf{0}\end{bmatrix}\mathbf{T}\mathbf{d}_{\mathrm{m}}, \tag{56}$$

where

$$\begin{bmatrix}\mathbf{u}\\ \mathbf{h}\end{bmatrix} = \mathbf{T}\mathbf{d}_{\mathrm{m}}, \tag{57}$$

and $\mathbf{h} = [\overline{H}_{11}, \overline{H}_{12}, \overline{H}_{13}, \overline{H}_{21}, \ldots, \overline{H}_{33}]^T$.

Deformation Under Uniaxial Loading

Finally, assuming that the deformation is applied quasi-statically, the equilibrium equations for the extruded unit cell can be obtained as

$$\frac{\partial E_{\mathrm{potential}}}{\partial \mathbf{u}} = 0, \tag{58}$$

where $E_{\text{potential}} = E_{\text{elastic}} - W$, $W = \mathbf{h}^T\mathbf{r}$ being the external work [46], for which we have defined $\mathbf{r} = \left[(\mathbf{r}^{v_1})^T, (\mathbf{r}^{v_2})^T, (\mathbf{r}^{v_3})^T\right]^T$. It follows from Eqs. (54)-(58) that

$$\mathbf{T}^T\left(\begin{bmatrix}\mathbf{J}_{\text{h}} & \mathbf{0}\end{bmatrix}^T\mathbf{K}_{\text{h}}\begin{bmatrix}\mathbf{J}_{\text{h}} & \mathbf{0}\end{bmatrix} + \begin{bmatrix}\mathbf{J}_{\text{st}} & \mathbf{0}\end{bmatrix}^T\mathbf{K}_{\text{st}}\begin{bmatrix}\mathbf{J}_{\text{st}} & \mathbf{0}\end{bmatrix} + \begin{bmatrix}\mathbf{J}_{\text{sh}} & \mathbf{0}\end{bmatrix}^T\mathbf{K}_{\text{sh}}\begin{bmatrix}\mathbf{J}_{\text{sh}} & \mathbf{0}\end{bmatrix} + \begin{bmatrix}\mathbf{J}_{\text{b}} & \mathbf{0}\end{bmatrix}^T\mathbf{K}_{\text{b}}\begin{bmatrix}\mathbf{J}_{\text{b}} & \mathbf{0}\end{bmatrix}\right)\mathbf{T}\mathbf{d}_{\text{m}} = \mathbf{T}^T\begin{bmatrix}\mathbf{0}\\ \mathbf{r}\end{bmatrix}. \tag{59}$$

Having determined the equilibrium equations for an extruded unit cell, we apply a uniaxial loading to the system by imposing $\overline{H}_{11} \neq 0$ and $\overline{H}_{ij} = 0$ for $i \neq j$, while leaving $\overline{H}_{22}$ and $\overline{H}_{33}$ unset (i.e. allowing the structure to freely expand in the lateral directions, while constraining macroscopic shear deformations). Note that we also constrained rigid body translations by fixing the displacement of a single vertex of the unit cell. To determine the response of the architected material along all directions, we rotate the unit cell about two axis according to

$$\mathbf{x}' = \mathbf{R}_z\mathbf{R}_{y'}\mathbf{x}, \tag{60}$$

in which

$$\mathbf{R}_z = \begin{bmatrix}\cos\gamma & -\sin\gamma & 0\\ \sin\gamma & \cos\gamma & 0\\ 0 & 0 & 1\end{bmatrix}, \tag{61}$$

$$\mathbf{R}_{y'} = \cos\theta\mathbf{I} + \sin\theta\begin{bmatrix}0 & -y_3' & y_2'\\ y_3' & 0 & -y_1'\\ -y_2' & y_1' & 0\end{bmatrix} + (1-\cos\theta)\begin{bmatrix}(y_1')^2 & y_1'y_2' & y_1'y_3'\\ y_2'y_1' & (y_2')^2 & y_2'y_3'\\ y_3'y_1' & y_3'y_2'(y_3')^2 & \end{bmatrix} \tag{62}$$

with $\mathbf{y}' = \mathbf{R}_z\mathbf{e}_y$ (see schematic in Supplementary Fig. 10). For each direction, we can determine the stiffness according to

$$K = \overline{s}_{11}/(\overline{H}_{11}). \tag{63}$$

[41] Laliberté, T. & Gosselin, C. Construction, mobility analysis and synthesis of polyhedra with articulated faces. *J. Mechanisms Robotics* **6**, 011007 (2013).

[42] Cook, R. *Concepts and applications of finite element analysis* (Wiley, 2001).

[43] Wei, Z. Y., Guo, Z. V., Dudte, L., Liang, H. Y. & Mahadevan, L. Geometric mechanics of periodic pleated origami. *Phys. Rev. Lett.* **110**, 215501 (2013).

[44] Schenk, M. & Guest, S. D. Geometry of miura-folded metamaterials. *Proc. Natl. Acad. Sci. U.S.A.* **110**, 3276-3281 (2013).

[45] Filipov, E. T., Tachi, T. & Paulino, G. H. Origami tubes assembled into stiff, yet reconfigurable structures and metamaterials. *Proc. Natl. Acad. Sci. U.S.A.* **112**, 12321-12326 (2015).

[46] Danielsson, M., Parks, D. & Boyce, M. Three-dimensional micromechanical modeling of voided polymeric materials. *J. Mech. Phys. Solids* **50**, 351-379 (2002).

[47] Gruñbaum, B. Uniform tilings of 3-space. *Geombinatorics* **4**, 49-56 (1994).

SUPPLEMENTAL FIGURES

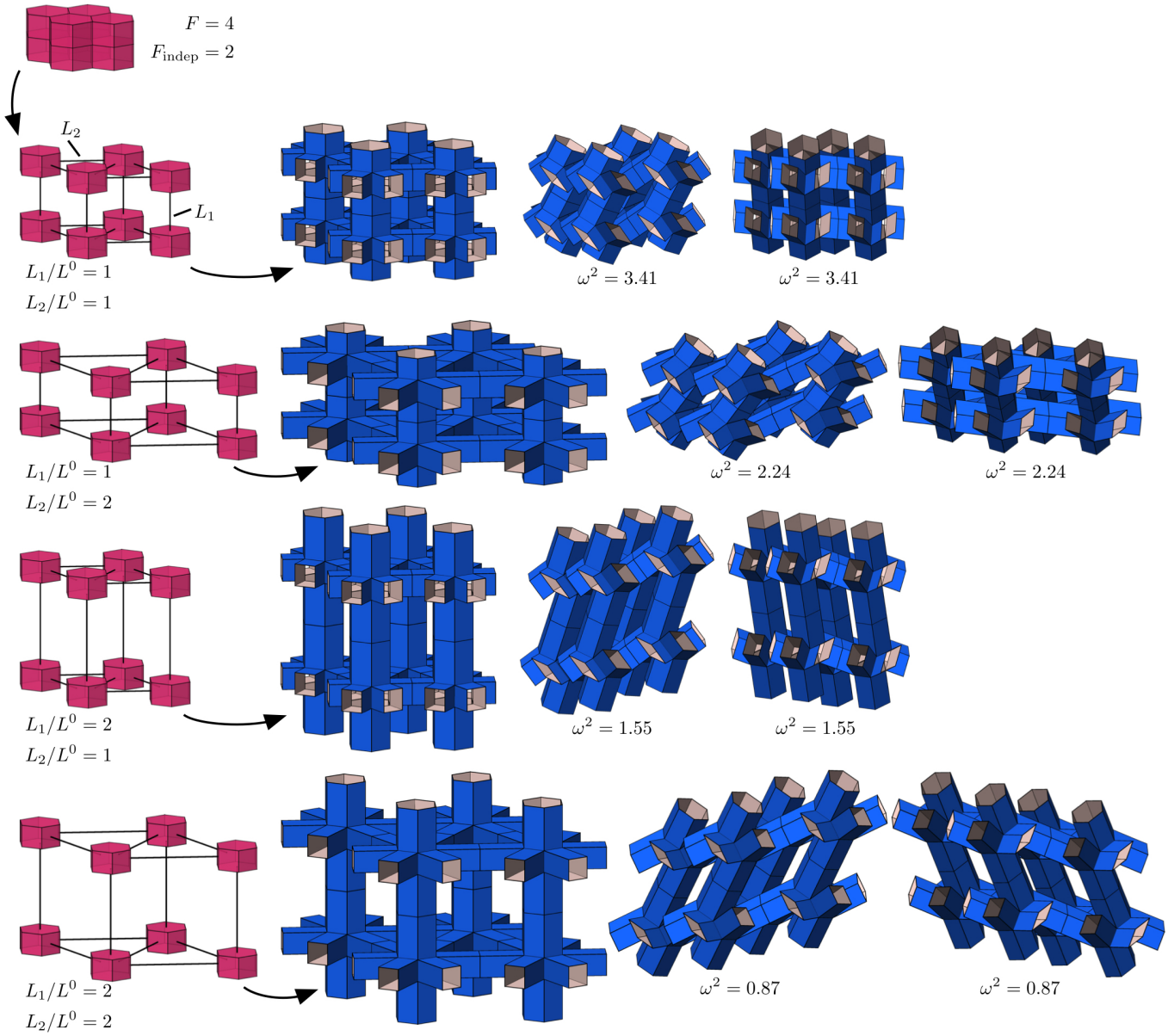

Supplementary Fig. 6: For a unit cell with F face pairs the expanded configuration is fully determined by choosing $F_{indep} \leq F$ extrusion lengths. As an example, here we consider four prismatic architected materials based on the space-filling assembly of hexagonal prisms (for which $F = 4$ and $F_{\text{indep}} = 2$) and show the effect of the two independent extrusions lengths L_1/L^0 and L_2/L^0 on the final extruded shape, in which L^0 denotes the length of the edges of the polyhedra. All four designs considered here have the same degrees of freedom ($n_{\text{dof}} = 2$).

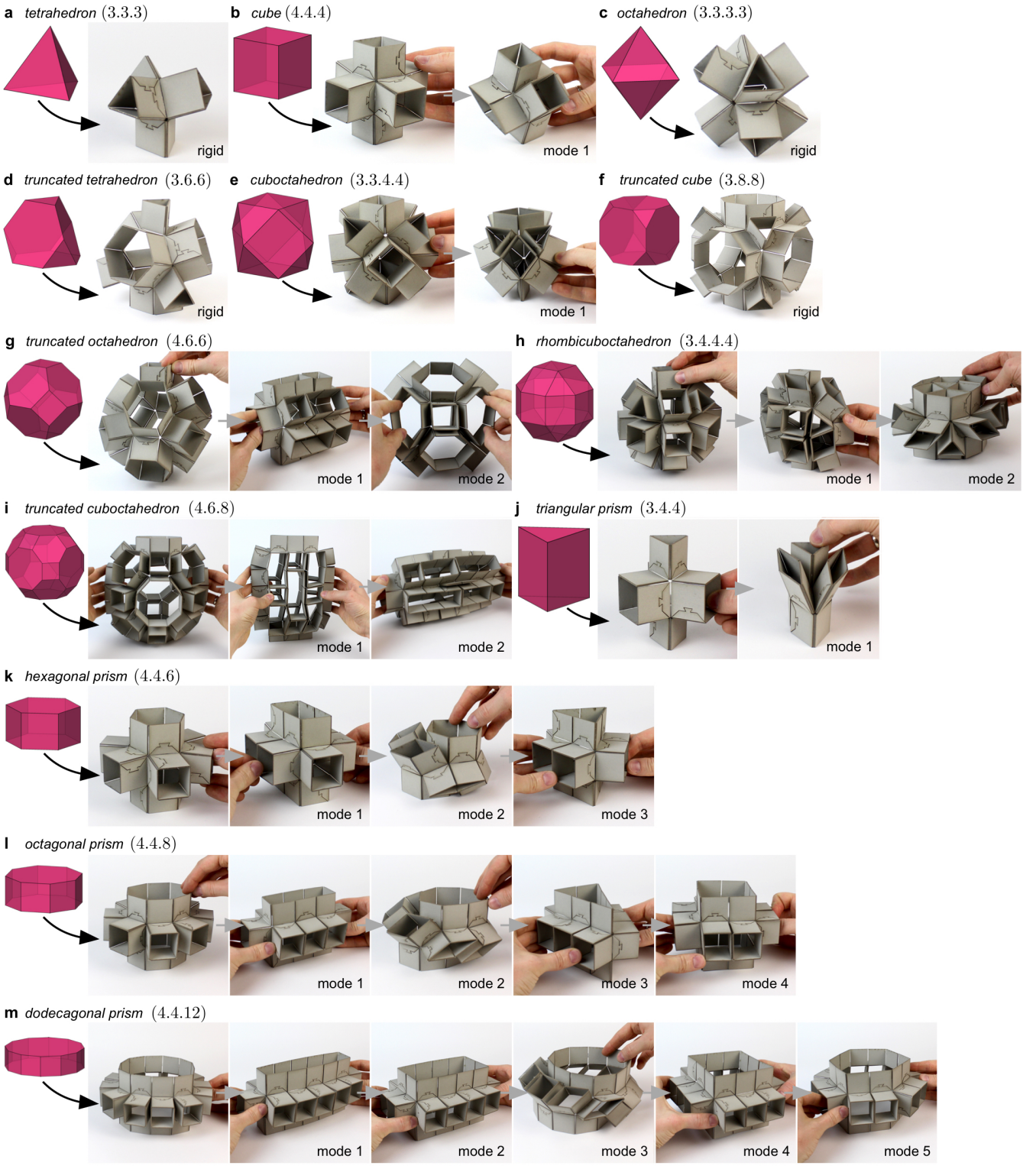

Supplementary Fig. 7: Reconfigurability of individual extruded polyhedra. The extruded units based on a (a) tetrahedron, (c) octahedron, (d) truncated tetrahedron and (f) truncated cube are rigid, while those based on the (b) cube, (e) cuboctahedron, (g) truncated octahedron, (h) rhombicuboctahedron, (i) truncated cuboctahedron, and (j-m) prisms are reconfigurable. For reference, we also denoted the polyhedra on which the unit cells are based by their Schäfli symbols. Note that only a selected number of deformation modes is shown, as it is not straightforward to determine all of them experimentally. For all the prototypes the edges are 35 mm.

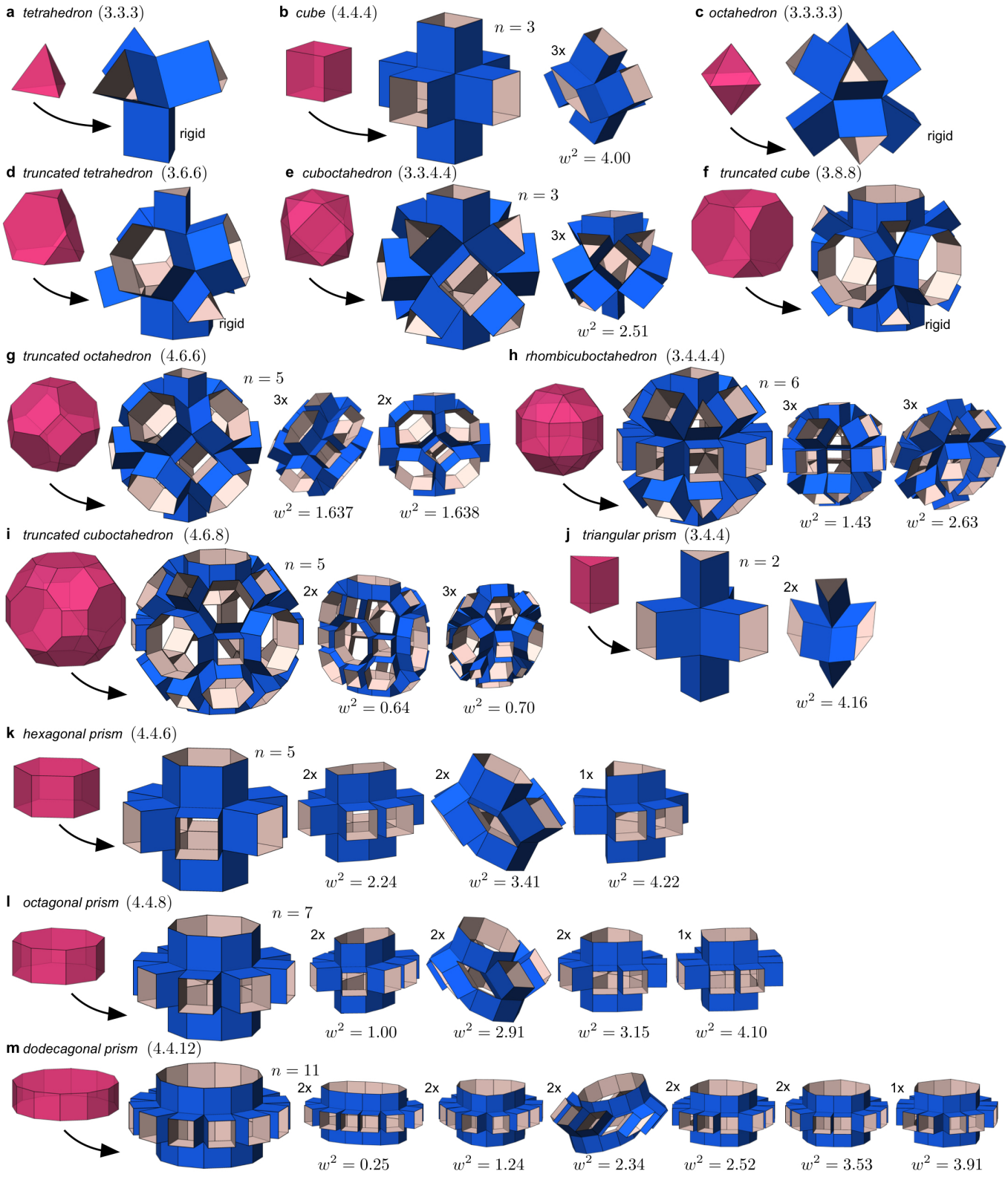

Supplementary Fig. 8: Numerically determined modes of individual extruded polyhedra. The extruded geometries based on the (a) tetrahedron, (c) octahedron, (d) truncated tetrahedron and (f) truncated cube are rigid, while those based on the (b) cube, (e) cuboctahedron, (g) truncated octahedron, (h) rhombicuboctahedron, (i) truncated cuboctahedron, and (j-m) prisms are reconfigurable. Importantly, using our numerical algorithm we can easily identify the degrees of freedom, n, and the deformation modes for the extruded units. Note that modes characterized by the same eigenvalue ω^2 are identical, so that we only show one of these modes. For reference, we also denoted the polyhedra on which the unit cells are based by their Schäfli symbols.

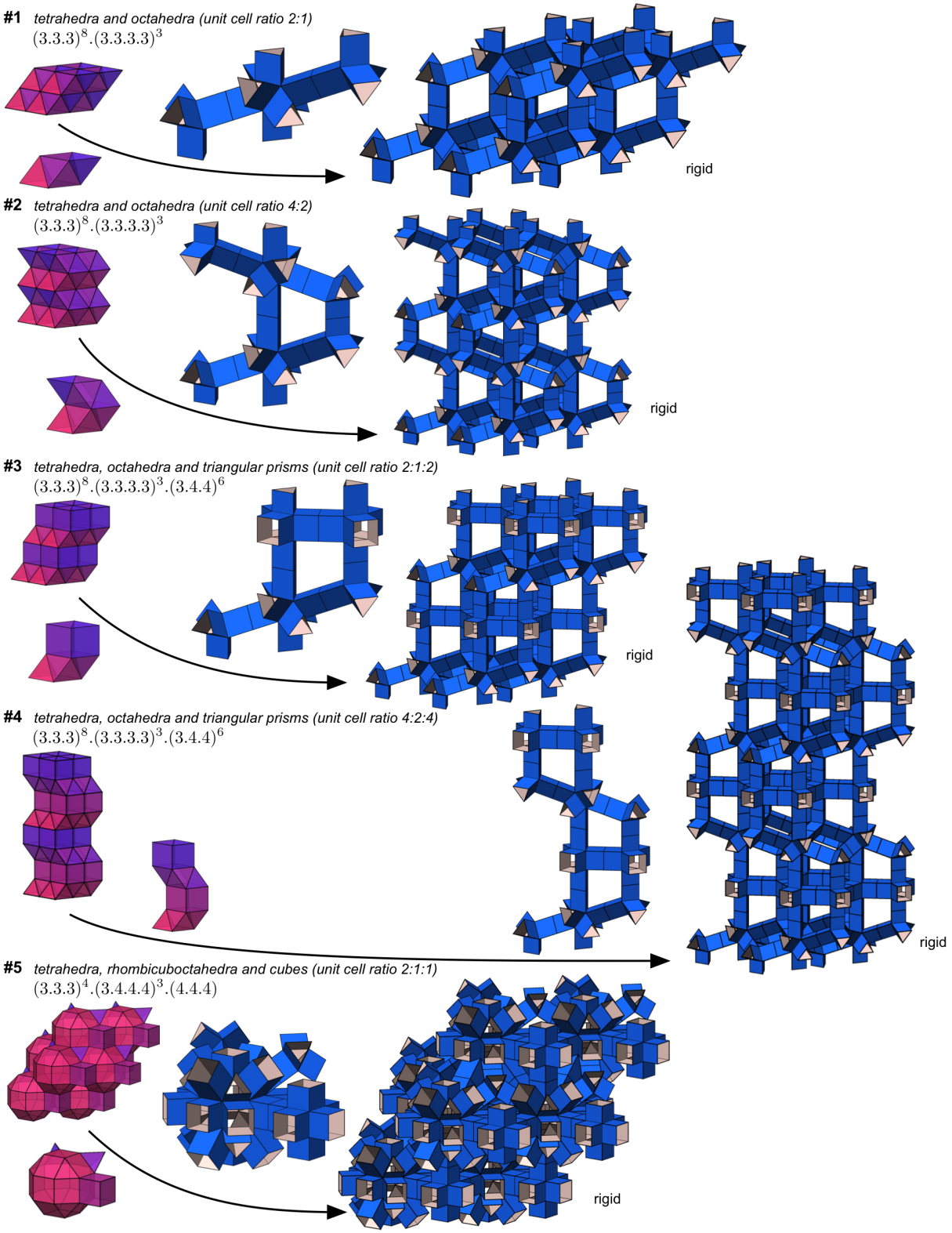

Supplementary Fig. 9: Reconfigurability of architected materials based on on the 28 uniform tessellations of the 3D space, which comprise regular polyhedra, semiregular polyhedra and semiregular prisms. The tessellations used as a template are indicated with the notation introduced in [47]. Specifically, the individual polyhedra are indicated by their Schäfli symbol, and the superscript shows the number of polyhedra of the given kind that meet at each vertex. Moreover, we also provide the number of each kind of polyhedra in the unit cell. (#1-2) The architected materials based on $(3.3.3)^8.(3.3.3.3)^6$ (tetrahedra and octahedra) are rigid. Note that #2 differs from #1 as it comprises reflected layers of tetrahedra and octahedra. (#3-4) The assemblies based on $(3.3.3)^8.(3.3.3.3)^3.(3.4.4)^6$ (tetrahedra, octahedra and triangular prisms) are rigid. Note that #4 differs from #3 as it comprises reflected layers of tetrahedra, octahedra and triangular prisms. (#5) $(3.3.3)^4.(3.4.4.4)^3.(4.4.4)$ (tetrahedra, rhombicuboctahedra and cubes) is rigid.

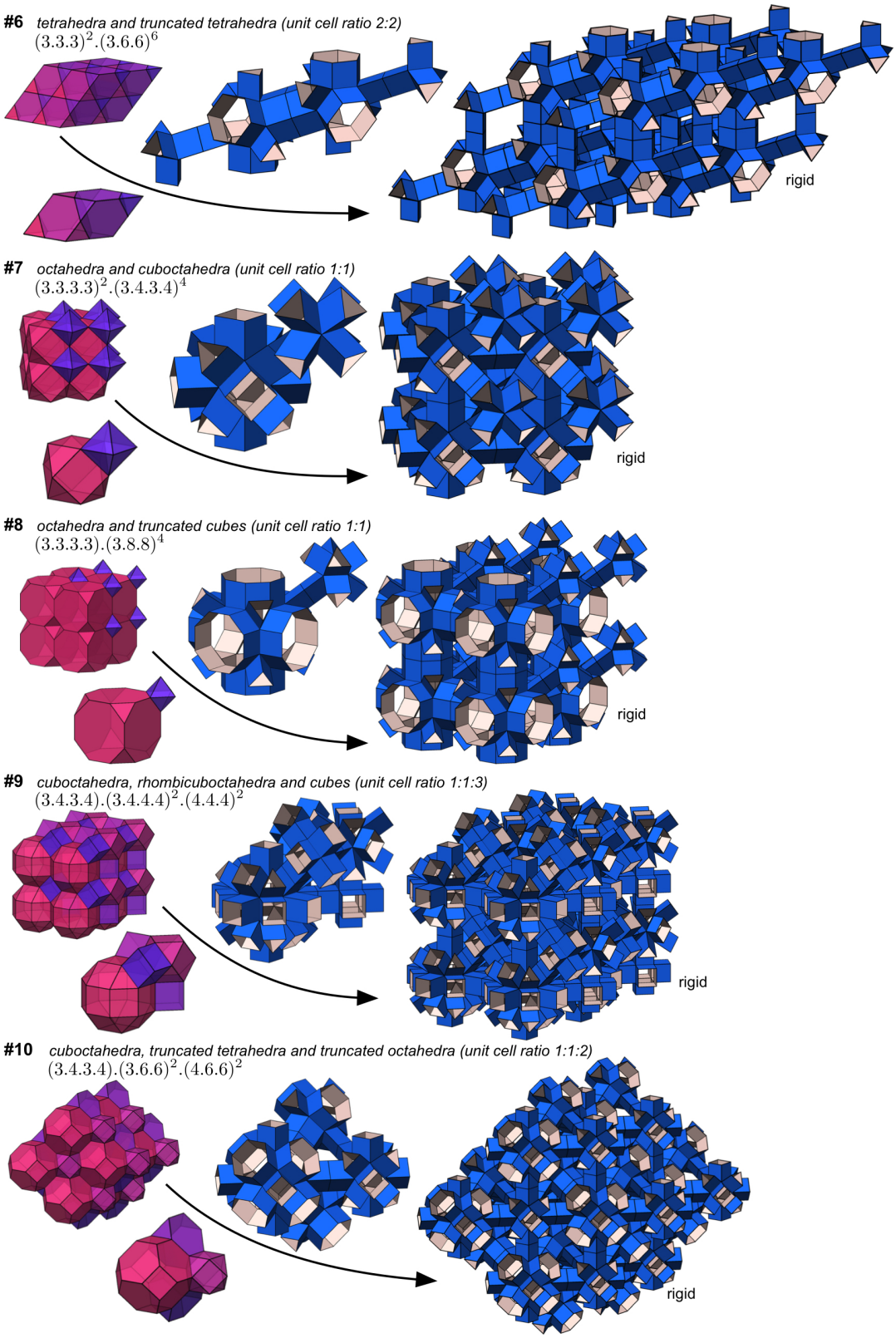

Supplementary Fig. 9: (continued). (#6) $(3.3.3)^2.(3.6.6)^6$ (tetrahedra and truncated octahedra) is rigid. (#7) $(3.3.3.3)^2.(3.4.3.4)^4$ (octahedra and cuboctahedra) is rigid. (#8) $(3.3.3.3).(3.8.8)^4$ (octaheda and truncated octahedra) is rigid. (#9) $(3.4.3.4).(3.4.4.4)^2.(4.4.4)^2$ (cuboctahedra, rhombicuboctahedra and cubes) is rigid. (#10) $(3.4.3.4).(3.6.6)^2.(4.6.6)^2$ (cuboctahedra, truncated tetrahedra and truncated octahedra) is rigid.

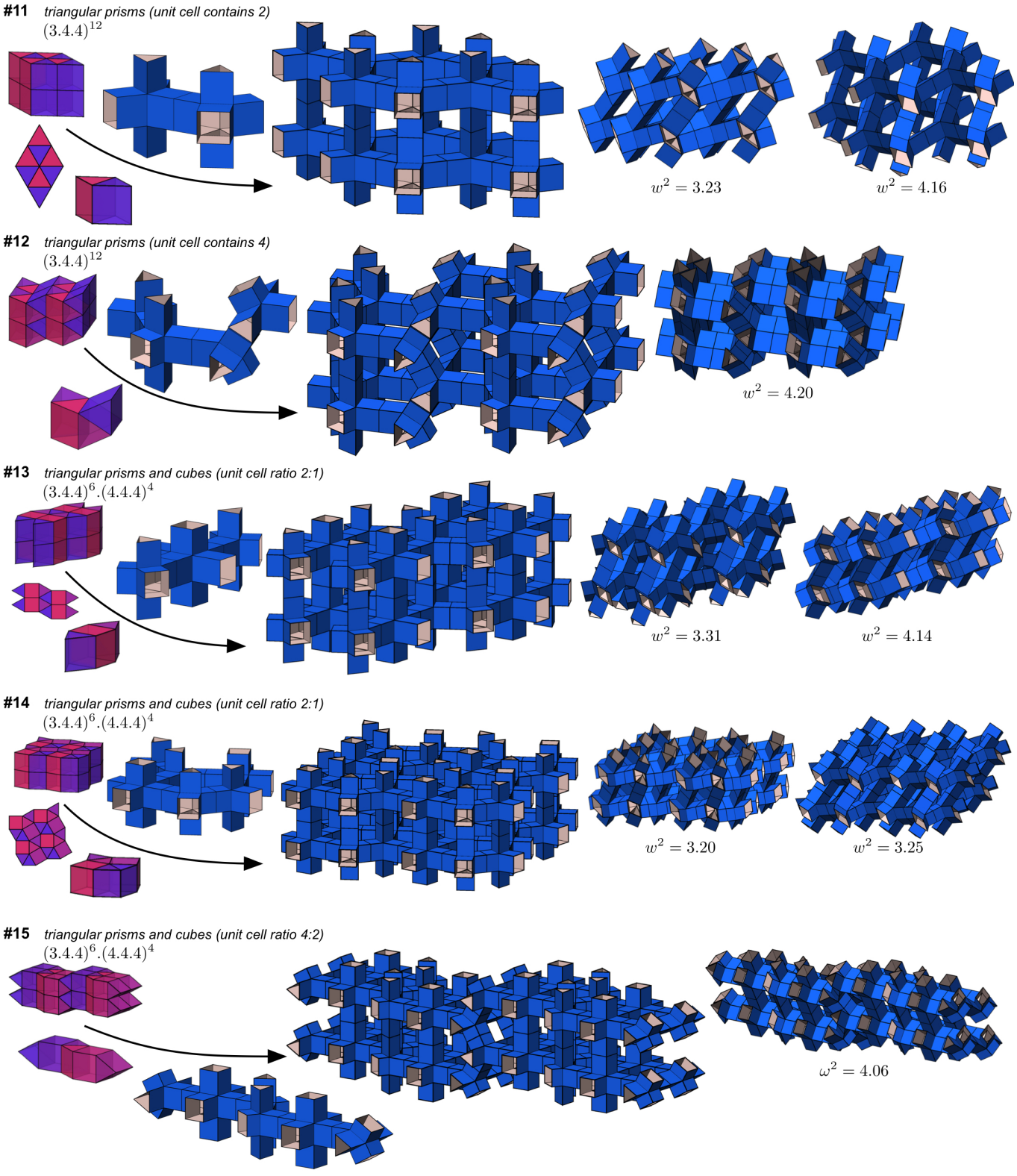

Supplementary Fig. 9: (continued). (#11-12) $(3.4.4)^{12}$ (triangular prisms) are reconfigurable with $n_{\mathrm{dof}} = 2$ and $n_{\mathrm{dof}} = 1$, respectively. Note that #12 differs from #11 as it comprises reflected layers of triangular prisms. (#13-15) $(3.4.4)^6.(4.4.4)^4$ (triangular prisms and cubes) are reconfigurable with $n_{\mathrm{dof}} = 2$, $n_{\mathrm{dof}} = 2$ and $n_{\mathrm{dof}} = 1$, respectively. Note that #14 differs from #13 as the polyhedra are differently arranged in-plane, and #15 differs from #13 as it comprises reflected layers of triangular prisms and cubes.

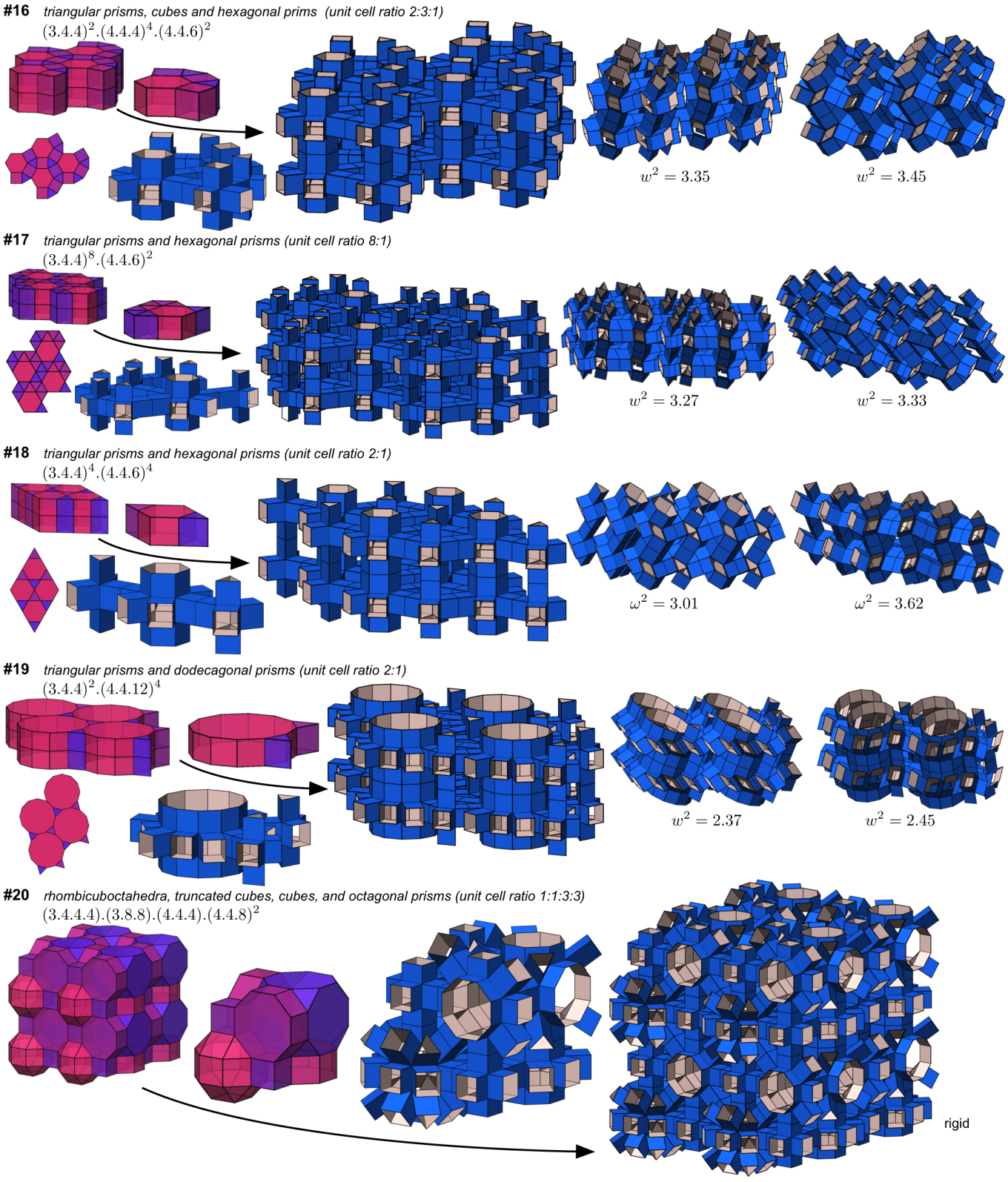

Supplementary Fig. 9: (continued). (#16) $(3.4.4)^2.(4.4.4)^4.(4.4.6)^2$ (triangular prisms, cubes and hexagonal prisms) is reconfigurable with $n_{\mathrm{dof}} = 2$. (#17) $(3.4.4)^8.(4.4.6)^2$ (triangular prisms and hexagonal prisms) is reconfigurable with $n_{\mathrm{dof}} = 2$. (#18) $(3.4.4)^4.(4.4.6)^4$ (triangular prisms and hexagonal prisms) is reconfigurable with $n_{\mathrm{dof}} = 2$. (#19) $(3.4.4)^2.(4.4.12)^4$ (triangular prisms and dodecagonal prisms) is reconfigurable with $n_{\mathrm{dof}} = 2$. (#20) $(3.4.4.4).(3.8.8).(4.4.4).(4.4.8)^2$ (rhombicuboctahedra, truncated cubes, cubes and octagonal prisms) is rigid.

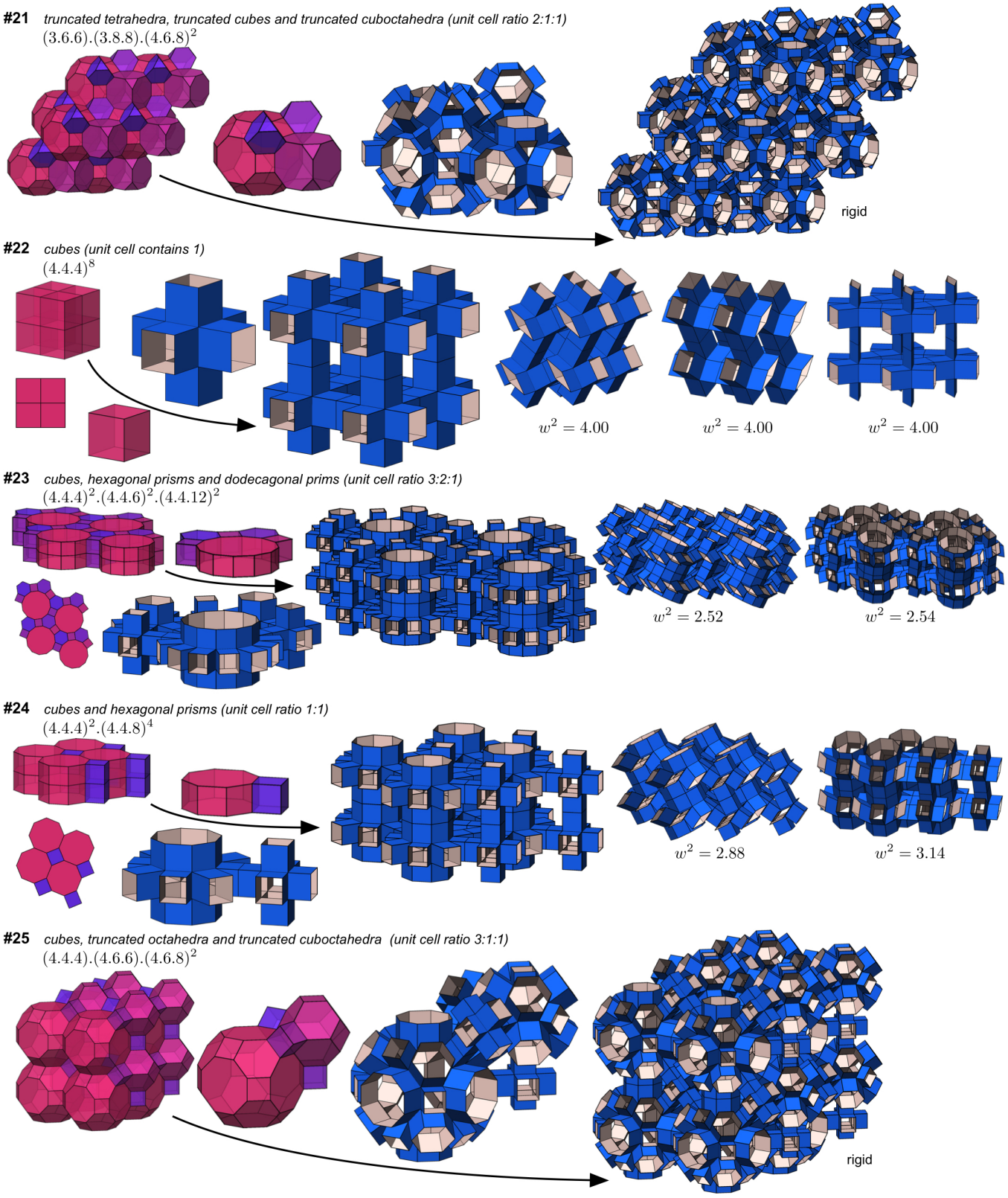

Supplementary Fig. 9: (continued). (#21) $(3.6.6).(3.8.8).(4.6.8)^2$ (truncated tetrahedra, truncated cubes and truncated cuboctahedra) is rigid. (#22) $(4.4.4)^8$ (cubes) is reconfigurable with $n_{\mathrm{dof}} = 3$. (#23) $(4.4.4)^2.(4.4.6)^2.(4.4.12)^2$ (cubes, hexagonal prisms and dodecagonal prisms) is reconfigurable with $n_{\mathrm{dof}} = 2$. (#24) $(4.4.4)^2.(4.4.8)^4$ (cubes and hexagonal prisms) is reconfigurable with $n_{\mathrm{dof}} = 2$. (#25) $(4.4.4).(4.6.6).(4.6.8)^2$ (cubes, truncated octahedra and truncated cuboctahedra) is rigid.

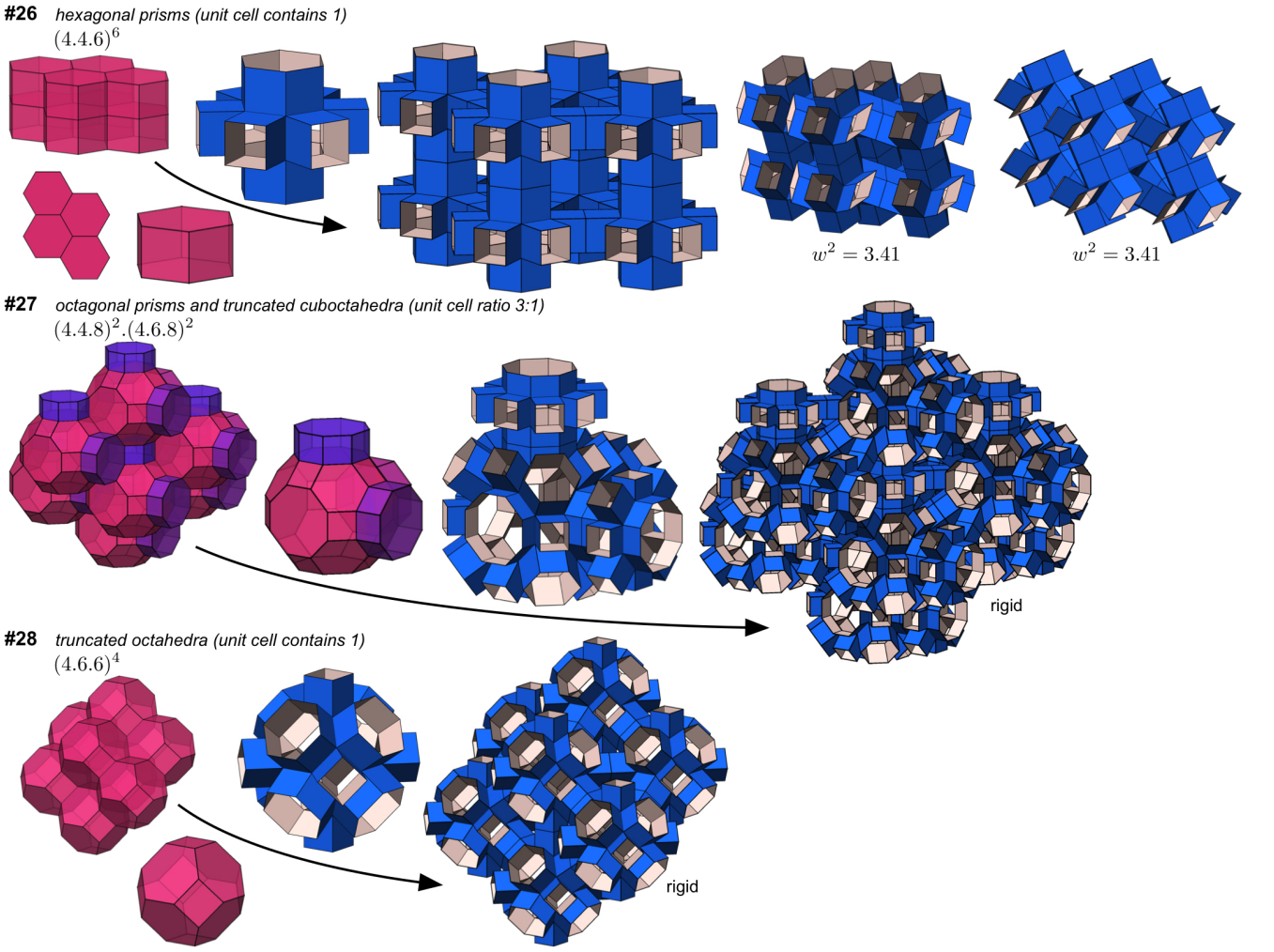

Supplementary Fig. 9: (continued). (#26) $(4.4.6)^6$ (hexagonal prisms) is reconfigurable with $n_{\mathrm{dof}} = 2$. (#27) $(4.4.8)^2.(4.6.8)^2$ (octagonal prisms and truncated cuboctahedra) is rigid. (#28) $(4.6.6)^4$ (truncated octahedra) is rigid.

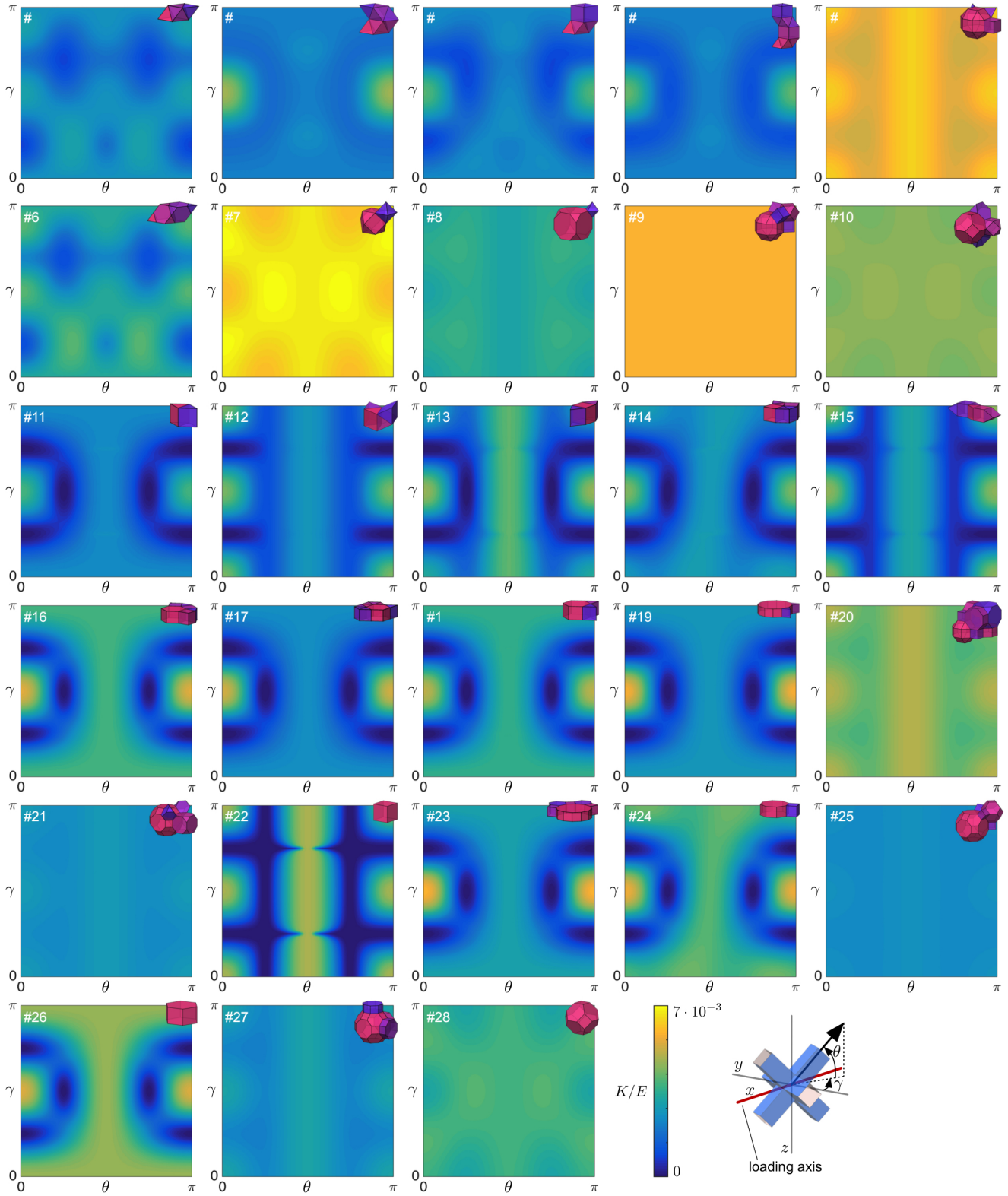

Supplementary Fig. 10: Normalized stiffness K/E of the 28 architected materials based on the uniform space-filling polyhedra assemblies. To determine the stiffness in all loading directions, the architected materials are rotated by angles γ and θ prior to loading.

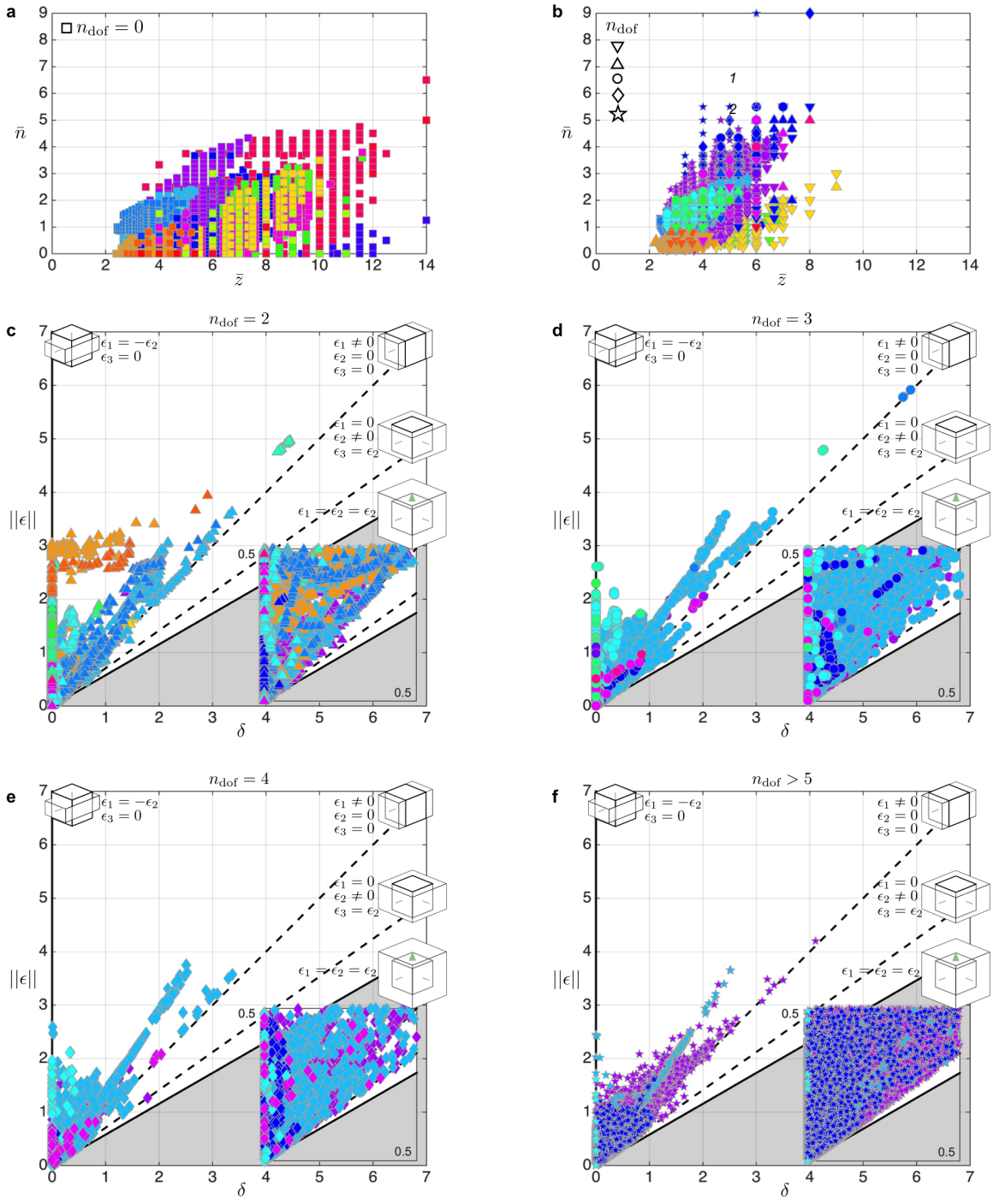

Supplementary Fig. 11: (a-b) Number of degrees of freedom, n_{dof}, for the altered architected materials based on the 28 uniform space-filling tessellations. Each point represents a design in which some of the faces of the unit cell are made rigid, instead of extruded. (c-f) Relation between the volumetric strain, δ, and the magnitude of the principal strains, $||\epsilon||$, for all the architected materials characterized by $n_{dof} = 2$, 3, 4 and > 5, respectively (Note that the results for $n_{dof} = 1$ are shown in Fig. 6). The color of the markers refers to the uniform tessellation that has been used as a template, as shown in Fig. 3.

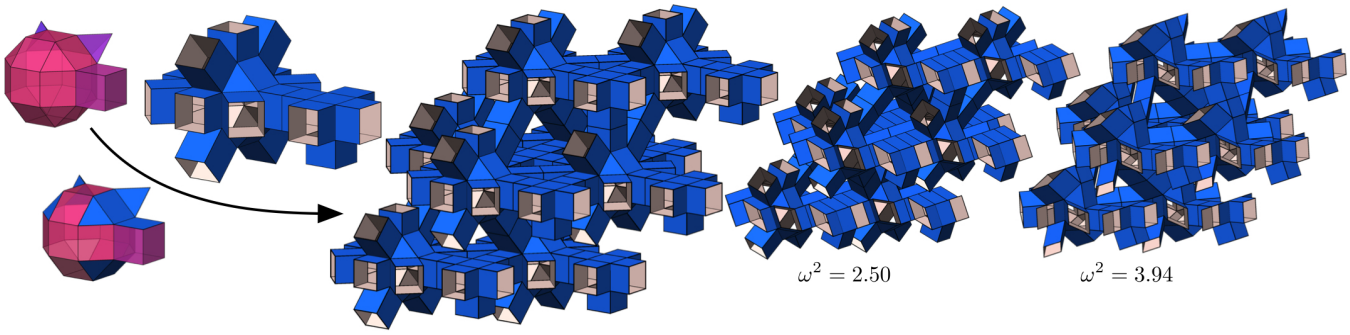

Supplementary Fig. 12: One of the six reconfigurable prismatic architected materials characterized by $\bar{z} = 9$ that we found using the numerical algorithm. This specific architected material is based on #5, for which 18 faces of the polyhedra are extruded and the remaining 18 faces are made rigid. Note that the faces of both tetrahedra are made fully rigid, and therefore are not taken into account in the numerical analysis. The resulting architected material has $n_{\mathrm{dof}} = 2$.

SUPPLEMENTAL TABLES

Supplementary Table 1: To enhance the reconfigurability of the proposed architected materials, we reduce their connectivity by selectively extruding faces of the unit cell, while making the remaining faces rigid. In this table we summarize the results obtained for the extruded structures based on the 28 uniform space-filling tessellations depicted in Fig. 3 and Supplementary Fig. 9. For this study we considered a maximum of 2^{16} designs per tessellation, randomly selected from the 2^F possibilities (where F is the number of face pairs), so that for 11 of the tessellations (#4-5, #9-10, #16-17, #20-21, #23, #25, and #27) the results are not complete, but rather indicate a trend. When determining the degrees of freedom, n_{dof}, we only consider the designs that do not contain any disconnected parts. However, we expanded the number of possible designs by removing the polyhedra for which all faces have been made rigid from the extruded unit cell, as those would have resulted in rigid parts completely disconnected from the architected materials.

unit cell	#designs	connected	percentage of connected with n_{dof}								
			$n_{\text{dof}}=0$	1	2	3	4	5	6	7	$>7, <17$
#1	2^8	24.7%	100.0%	0	0	0	0	0	0	0	0
#2	2^{13}/ 2^{16}	24.8%	100.0%	0	0	0	0	0	0	0	0
#3	2^{13}	16.7%	62.5%	34.0%	3.5%	0	0	0	0	0	0
#4	2^{13}/ 2^{26}	15.3%	62.1%	33.6%	4.3%	0	0	0	0	0	0
#5	2^{13}/ 2^{20}	91.6%	96.6%	3.2%	0.230%	0	0	0	0	0	0
#6	2^{12}	45.2%	100.0%	0	0	0	0	0	0	0	0
#7	2^{11}	66.1%	100.0%	0	0	0	0	0	0	0	0
#8	2^{11}	66.9%	100.0%	0	0	0	0	0	0	0	0
#9	2^{13}/ 2^{29}	94.4%	99.8%	0.249%	0	0	0	0	0	0	0
#10	2^{13}/ 2^{22}	96.4%	100.0%	0	0	0	0	0	0	0	0
#11	2^5	12.9%	0	0	100.0%	0	0	0	0	0	0
#12	2^{10}	9.9%	0	81.2%	17.8%	0.990%	0	0	0	0	0
#13	2^8	11.4%	0	0	75.9%	24.1%	0	0	0	0	0
#14	2^{13}/ 2^{16}	13.1%	43.7%	34.6%	19.6%	2.0%	0.070%	0	0	0	0
#15	2^{13}/ 2^{16}	3.1%	0	36.1%	43.8%	16.9%	3.0%	0.194%	0	0	0
#16	2^{13}/ 2^{18}	28.9%	36.5%	31.4%	18.7%	8.6%	3.8%	0.909%	0.048%	0	0
#17	2^{13}/ 2^{24}	11.4%	61.7%	31.1%	7.0%	0.175%	0	0	0	0	0
#18	2^9	26.8%	27.7%	66.4%	5.8%	0	0	0	0	0	0
#19	2^{12}	52.9%	46.3%	7.3%	9.6%	7.0%	5.5%	12.5%	0	11.9%	0
#20	2^{13}/ 2^{44}	99.0%	100.0%	0.002%	0	0	0	0	0	0	0
#21	2^{13}/ 2^{28}	99.5%	100.0%	0	0	0	0	0	0	0	0
#22	2^3	28.6%	0	0	0	100.0%	0	0	0	0	0
#23	2^{13}/ 2^{24}	60.1%	28.6%	20.0%	12.7%	9.8%	7.3%	5.2%	4.4%	3.3%	8.6%
#24	2^8	44.3%	18.6%	42.5%	9.7%	15.0%	14.2%	0	0	0	0
#25	2^{13}/ 2^{29}	93.4%	100.0%	0	0	0	0	0	0	0	0
#26	2^4	33.3%	0	0	40.0%	60.0%	0	0	0	0	0
#27	2^{13}/ 2^{28}	97.2%	100.0%	0	0	0	0	0	0	0	0
#28	2^7	62.2%	94.9%	5.1%	0	0	0	0	0	0	0